Mixed shell element for static and buckling analysis of variable angle tow composite plates

G. Zucco[b], RMJ Groh[a], A Madeo[b,*], PM Weaver[a]

[a]*ACCIS, University of Bristol, Queen's Building, University Walk, Bristol, BS8 1 TR, UK*
[b]*DIMES, University of Calabria, Ponte P. Bucci Cubo, 87036 Rende (Cosenza), Italy*

Abstract

A mixed quadrilateral 3D finite element, obtained from the Hellinger-Reissner functional, is presented for linear static and buckling analyses of variable-angle tow (VAT) composite plates. Variable-angle tows describe curvilinear fiber paths within composite laminae and are a promising technology for tailoring the buckling and post-buckling capability of plates. Due to the variable stiffness across the planform of the VAT plates, pre-buckling stresses can be tailored and redistributed towards supported edges, thereby greatly improving the buckling load. A linear mixed element called MISS-4 is used as starting point for this work. The element presents a self-equilibrated and isostatic state of stress. The kinematics lead to element compatibility matrix calculations based solely on the interpolation along element edges. The drilling rotations do not require penalty functions or non-symmetric formulations, thus avoiding spurious energy modes. The buckling analysis is reliably performed via a co-rotational formulation. In this work VAT plates with linear fibre angle variation in one direction, and constant stiffness properties in the orthogonal direction are studied. Numerical examples of VAT plates subjected to different loads and boundary conditions are investigated herein. The convergence of displacements, stress resultants and buckling loads are presented, and comparisons with numerical results, obtained using the S4R finite element of Abaqus and the pseudo-spectral differential quadrature method, are shown.

Keywords: Composite plates, variable angle tow, mixed finite element, Hellinger-Reissner, static and buckling analyses.

1. INTRODUCTION

Thin-walled structures are the most widely used form of construction in a number of different engineering applications, ranging from fuselages and wings in the aerospace industry aerospace to car panels in the automotive sector and ship hulls in the naval industry. In these applications the thin-walled construction allows the shape-defining outer skin of the body to become an active load-carrying member of the structure, thereby increasing the structural efficiency by combining aerodynamic and structural functions in one. Whereas thin-walled structures are efficient in carrying membrane loading, the thin-skinned construction means that compression and shear buckling become likely forms of failure.

Hence, a realistic evaluation of the structural performance of thin-walled structures requires nonlinear phenomena, such as the loss of stability, to be correctly accounted for [1]. Above all, in the case of careful structural optimization [2–7], multimodal buckling interaction [8] can induce complex post-critical behavior that strongly affects the load carrying capacity [9]. In this case the sensitivity of the structural behavior to imperfections has to be carefully investigated.

*Corresponding author. antonio.madeo81@unical.it

The finite element implementation of Koiter's analysis, as developed over the last thirty years by Casciaro et al. [1], offers a robust and efficient way to analyze thin-walled structures. The method allows an accurate recovery of pre-critical, critical and initial post-critical behavior even in the presence of strong multimodal buckling interactions. Furthermore, it allows an efficient imperfection sensitivity analysis when coupled with Monte Carlo simulations [10, 11].

The implementation of the method requires the structural model to be geometrically exact [12–14] almost up to the fourth order required for the asymptotic expansion of Koiter's implementation proposed by Casciaro [1] (see also [15] and [16] for the case of 3D-beam and plate models, respectively). The use of corotational algebra allows the fulfillment of these requirements by simply starting from a linear structural model at the continuum level or from a linear finite element in a numerical context [13]. The use of a mixed formulation guarantees the overall effectiveness of the method [17] avoiding extrapolation locking [18].

Due to their high specific strength and specific stiffness properties, the use of multilayered composites in load-bearing structures is on the rise. In this respect, variable angle tow (VAT) composites are a promising technology for further improving the structural efficiency of engineering structures due to the increased design space available for tailoring. In these variable stiffness structures the fibre tows within one layer are not restricted to straight trajectories but can describe curvilinear paths. VAT plates and shells are manufactured by automated fibre laying technologies such as Automated Fibre Placement and the Continous Tow Shearing process, which each have certain practical limitations regarding the extent of fibre steering and manufacturing defects [19].

The idea of tailoring the structural performance of composite laminates by spatially varying the pointwise fibre orientations has been explored since the early 1970's [20]. Numerous works have shown that tailoring the in-plane stiffness over the plate planform allows prebuckling stresses to be redistributed to supported regions, thereby increasing the critical buckling load [21–27]. Specifically, Gürdal et al. [22] have shown that varying the stiffness of the panel perpendicular to the direction of applied end compression results in greater improvements than varying the stiffness in the direction of loading. Furthermore, Coburn et al. [28] investigated the concept of using VAT technology to design blade-stiffened wing panels with greater critical buckling loads.

Recent results show that VAT plates with linear fibre variations can be designed to exhibit smaller stiffness reductions in the postbuckling regime than their straight-fibre counterparts [29, 30]. In this regard, an interesting application of variable-stiffness composites is in designing cylindrical shells with stable postbuckling paths. White and Weaver [31] have shown that the imperfection sensitivity of curved shells can be effectively eliminated by tailoring the fibre paths across the surface of the cylindrical shell, thereby creating stable plate-like postbuckling responses.

Due to its modelling versatility and numerical robustness, most modelling work on the buckling of VAT structures has focused on using the classic weak-form Finite Element Method (FEM) [23, 32–35]. Higher-order finite elements have also been used to study the bending [36] and vibrational response [37, 38] of VAT plates. At the same time, the pseudo-spectral Differential Quadrature Method (DQM) has been shown to be a fast, accurate and computationally efficient technique for solving the variable-coefficient higher-order differential equations for bending [39], buckling [26, 40] and postbuckling [27, 41] of VAT plates and cylindrical shells [42, 43]. For a recent review on the differential quadrature method the interested reader is directed to [44]. The work by White et al. [42], Raju et al. [45] and Groh & Weaver [43] has shown the efficiency and effectiveness of using Koiter's asymptotic analysis within a DQM framework to study the critical and post-critical behavior of VAT plates and shells. Furthermore, a strong-form finite element method based on DQM has been used to study the static [46] and vibrational response [47] of doubly-curved VAT laminates.

Our present aim is to develop a mixed finite element for the analysis of VAT composite plates. This, as previously stated, is the first step for the implementation of Koiter's asymptotic analysis of VAT composite plates. The starting point is the mixed flat shell finite element called MISS-4 [48–50](Mixed Isostatic Self-

Equilibrated Stress) which is introduced in Sections 2 and 3. The element has four nodes with six degrees of freedom per node including the drilling rotation. As the element is based on self-equilibrated stress assumptions, the kinematics need only be described on the element boundary. The assumed stress field is governed by 18 stress parameters (i.e. isostatic stress). The compatibility matrix is efficiently obtained by boundary integration. The compliance matrix is evaluated accounting for the VAT constitutive laws.

In Section 4 the present model is validated using the S4R element available in the commercial FEM code ABAQUS [51], and the DQM approach introduced above. The proposed MISS-4 finite element exhibits very good performance for both linear static analysis and buckling. Several tests show an h^2 convergence for point-wise stresses, displacements and buckling loads. Finally, conclusions are drawn in Section 5.

2. HELLINGER-REISSNER FORMULATION FOR VAT

The Hellinger-Reissner functional is

$$\Pi = \Phi - W_{ext} \tag{1}$$

where Φ is the mixed strain energy expressed in terms of stress resultants and generalized displacements and W_{ext} is the work done by external loads. Using the assumptions of first-order shear deformation theory and defining a Cartesian reference system $\{X, Y, Z\}$ with the Z-axis along the thickness direction the mixed strain energy of the plate can written as

$$\Phi[\boldsymbol{t}, \boldsymbol{u}] = \int_\Omega \left\{ \boldsymbol{t}^T \boldsymbol{D}\boldsymbol{d} - \frac{1}{2}\boldsymbol{t}^T \boldsymbol{E}^{-1}\boldsymbol{t} \right\} \mathrm{d}\Omega \qquad \boldsymbol{t} = \begin{bmatrix} \boldsymbol{t}_m \\ \boldsymbol{t}_f \end{bmatrix}, \quad \boldsymbol{d} = \begin{bmatrix} \boldsymbol{d}_m \\ \boldsymbol{d}_f \end{bmatrix}, \quad \boldsymbol{D} = \begin{bmatrix} \boldsymbol{D}_m & \boldsymbol{0} \\ \boldsymbol{0} & \boldsymbol{D}_f \end{bmatrix}$$

where Ω is the two-dimensional domain, vectors $\boldsymbol{t}_m$ and $\boldsymbol{t}_f$ are the classical membrane stress resultants and the bending/transverse shear stress resultants, respectively

$$\boldsymbol{t}_m = \begin{bmatrix} N_x \\ N_y \\ N_{xy} \end{bmatrix}, \quad \boldsymbol{t}_f = \begin{bmatrix} \boldsymbol{t}_b \\ \boldsymbol{t}_s \end{bmatrix} \quad \text{with} \quad \boldsymbol{t}_b = \begin{bmatrix} M_x \\ M_y \\ M_{xy} \end{bmatrix} \quad \text{and} \quad \boldsymbol{t}_s = \begin{bmatrix} S_x \\ S_y \end{bmatrix}. \tag{2}$$

The vectors $\boldsymbol{d}_m$ and $\boldsymbol{d}_f$ are the in- and out-of-plane generalized displacement variables

$$\boldsymbol{d}_m = \begin{bmatrix} d_x \\ d_y \end{bmatrix}, \quad \boldsymbol{d}_f = \begin{bmatrix} d_z \\ \varphi_x \\ \varphi_y \end{bmatrix}. \tag{3}$$

The differential operators $\boldsymbol{D}_m$ and $\boldsymbol{D}_f$ are defined as

$$\boldsymbol{D}_m = \begin{bmatrix} \partial/\partial X & 0 \\ 0 & \partial/\partial Y \\ \partial/\partial Y & \partial/\partial X \end{bmatrix}, \quad \boldsymbol{D}_f = \begin{bmatrix} 0 & 0 & -\partial/\partial X \\ 0 & \partial/\partial Y & 0 \\ 0 & \partial/\partial X & -\partial/\partial Y \\ \partial/\partial X & 0 & 1 \\ \partial/\partial Y & -1 & 0 \end{bmatrix}. \tag{4}$$

The constitutive matrix for a laminate with n VAT layers can be written as

$$\boldsymbol{E} = \begin{bmatrix} \boldsymbol{E}_m & \boldsymbol{E}_{mb} & \boldsymbol{0} \\ & \boldsymbol{E}_b & \boldsymbol{0} \\ \text{sym.} & & \boldsymbol{E}_s \end{bmatrix} \quad , \quad \begin{cases} \boldsymbol{E}_m = \displaystyle\sum_k^n (Z_k - Z_{k-1})\boldsymbol{E}_m^{(k)}, & \boldsymbol{E}_{mb} = \frac{1}{2}\displaystyle\sum_k^n (Z_k^2 - Z_{k-1}^2)\boldsymbol{E}_m^{(k)} \\ \boldsymbol{E}_b = \frac{1}{3}\displaystyle\sum_k^n (Z_k^3 - Z_{k-1}^3)\boldsymbol{E}_m^{(k)}, & \boldsymbol{E}_s = \boldsymbol{\kappa} \odot \displaystyle\sum_k^n (Z_k - Z_{k-1})\boldsymbol{E}_s^{(k)} \end{cases}$$

where Z_k, Z_{k-1} are the top and bottom coordinates of k-th lamina, respectively, $\boldsymbol{E}_m^{(k)}, \boldsymbol{E}_s^{(k)}$ are the lamina constitutive matrices referring to in-plane [52] and transverse stress/strain [53, Eq.(6.16)], respectively, which in the case of VAT are functions of the coordinates $(X,\ Y)$ (i.e. $\boldsymbol{E}_m^{(k)} = \boldsymbol{E}_m^{(k)}(X,\ Y)$, $\boldsymbol{E}_s^{(k)} = \boldsymbol{E}_s^{(k)}(X,\ Y)$). Finally, symbol $\odot$ denotes the component product (.* in [54]) that allows us to introduce different shear correction factors for each component of the $\boldsymbol{E}_s$ matrix [55, 56]

$$\boldsymbol{\kappa} = \begin{bmatrix} \kappa_{11} & \kappa_{12} \\ \kappa_{12} & \kappa_{22} \end{bmatrix}. \tag{5}$$

3. MISS-4 LINEAR FINITE SHELL ELEMENT

The geometry of the Mixed Isostatic Self-equilibrated Stress (MISS-4) element [48] is described by four nodal coordinates on the plane $Z = 0$ of the global Cartesian system $\{X,\ Y,\ Z\}$ and the element connectivity as shown in Fig. 1.

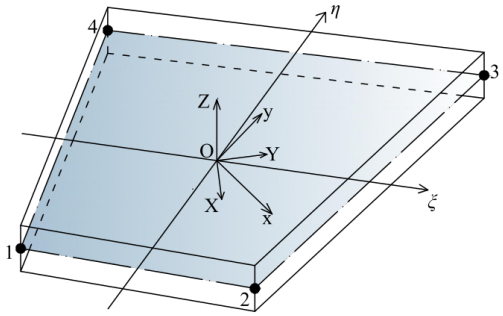

Figure 1: Global, local and internal coordinate systems.

Next, a dimensionless internal system is defined over the element midsurface with $\{\xi,\ \eta\}$, $-1 \le \xi \le 1, -1 \le \eta \le 1$, implicitly defined by

$$\begin{cases} X = a_0 + a_1\xi + a_2\xi\,\eta + a_3\eta \\ Y = b_0 + b_1\xi + b_2\xi\,\eta + b_3\eta \end{cases} \tag{6}$$

where

$$\begin{bmatrix} a_0 & b_0 \\ a_1 & b_1 \\ a_2 & b_2 \\ a_3 & b_3 \end{bmatrix} = \frac{1}{4}\begin{bmatrix} 1 & 1 & 1 & 1 \\ -1 & 1 & 1 & -1 \\ 1 & -1 & 1 & -1 \\ -1 & -1 & 1 & 1 \end{bmatrix}\begin{bmatrix} X_1 & Y_1 \\ X_2 & Y_2 \\ X_3 & Y_3 \\ X_4 & Y_4 \end{bmatrix} \tag{7}$$

and $\{X_i,\ Y_i\},\ i = 1, .., 4$ are the global nodal coordinates.

The third system is a local Cartesian system $\{x,\ y\}$, defined over the element mid surface, centered and aligned with the element. To define the local system, we introduce the Jacobian matrix $\boldsymbol{J}^G$ and its average $\bar{\boldsymbol{J}}^G$

$$\boldsymbol{J}^G = \begin{bmatrix} X_{,\xi} & X_{,\eta} \\ Y_{,\xi} & Y_{,\eta} \end{bmatrix} = \begin{bmatrix} (a_1 + a_2\eta) & (a_3 + a_2\xi) \\ (b_1 + b_2\eta) & (b_3 + b_2\xi) \end{bmatrix} \quad , \quad \bar{\boldsymbol{J}}^G = \frac{1}{4}\int_{\xi=-1}^{1}\int_{\eta=-1}^{1} \boldsymbol{J}^G\,\mathrm{d}\xi\,\mathrm{d}\eta = \begin{bmatrix} a_1 & a_3 \\ b_1 & b_3 \end{bmatrix}. \tag{8}$$

The average Jacobian $\bar{\boldsymbol{J}}^G$ is decomposed into an orthogonal matrix $\boldsymbol{R}$ and a symmetric matrix $\bar{\boldsymbol{J}}$ so that

$$\bar{\boldsymbol{J}}^G = \boldsymbol{R}\,\bar{\boldsymbol{J}} \tag{9}$$

with

$$\boldsymbol{R} = \begin{bmatrix} \cos\alpha & -\sin\alpha \\ \sin\alpha & \cos\alpha \end{bmatrix}, \quad \alpha = \arctan\left(\frac{a_3 - b_1}{a_1 + b_3}\right), \quad \bar{\boldsymbol{J}} = \begin{bmatrix} a & c \\ c & b \end{bmatrix} \tag{10}$$

with $a = a_1 \cos\alpha + b_1 \sin\alpha$, $b = -a_3 \sin\alpha + b_3 \cos\alpha$ and $c = a_3 \cos\alpha + b_3 \sin\alpha$. The local Cartesian system $\{x, y\}$ has its origin at the element centroid ($\xi = \eta = 0$) and is rigidly rotated by $\boldsymbol{R}$ with respect to $\{X, Y\}$. The coordinates $\{x, y\}$ are defined according the transformation

$$\begin{bmatrix} x \\ y \end{bmatrix} = \boldsymbol{R}^T \begin{bmatrix} X - a_0 \\ Y - b_0 \end{bmatrix}. \tag{11}$$

The use of a local system $\{x, y\}$ allows us to eliminate the rigid part of the global element distortion, providing a finite element description that is objective with respect to a rigid body motion of the element.

3.1. Assumed stresses

The stresses are assumed to be self-equilibrated and isostatic, leading to a minimum set of parameters [57], which are the 18 components of the vector $\boldsymbol{\beta}_e$. Then, the stress resultants can be written as

$$\boldsymbol{t} = \boldsymbol{B}\boldsymbol{\beta}_e = \begin{bmatrix} \boldsymbol{B}_m & \boldsymbol{0} \\ \boldsymbol{0} & \boldsymbol{B}_f \end{bmatrix} \begin{bmatrix} \boldsymbol{\beta}_m \\ \boldsymbol{\beta}_f \end{bmatrix} \tag{12a}$$

where $\boldsymbol{B}_m$ and $\boldsymbol{B}_f$ are matrices representing the assumed stress modes for the membrane and flexural generalized stresses, respectively, and $\boldsymbol{\beta}_m, \boldsymbol{\beta}_f$ are 9-component vectors representing membrane and flexural effects, respectively. For the membrane stresses it is assumed that

$$\boldsymbol{B}_m = \begin{bmatrix} 1 & 0 & 0 & y & 0 & x & 0 & y^2 & -2\,a^2\,x\,y \\ 0 & 1 & 0 & 0 & x & 0 & y & -x^2 & 2\,b^2\,x\,y \\ 0 & 0 & 1 & 0 & 0 & -y & -x & 0 & a^2\,y^2 - b^2\,x^2 \end{bmatrix}. \tag{12b}$$

For the flexural stress it is assumed that

$$\boldsymbol{B}_f = \begin{bmatrix} \boldsymbol{B}_b \\ \boldsymbol{B}_s \end{bmatrix} \quad \text{with} \quad \begin{cases} \boldsymbol{B}_b = \begin{bmatrix} 1 & 0 & 0 & x & 0 & y & 0 & x\,y & 0 \\ 0 & 1 & 0 & 0 & x & 0 & y & 0 & x\,y \\ 0 & 0 & 1 & 0 & y\,\bar{c} & x/\bar{c} & 0 & 0 & 0 \end{bmatrix} \\ \boldsymbol{B}_s = \begin{bmatrix} 0 & 0 & 0 & -1 & -\bar{c} & 0 & 0 & -y & 0 \\ 0 & 0 & 0 & 0 & 0 & -1/\bar{c} & -1 & 0 & -x \end{bmatrix} \end{cases} \tag{12c}$$

with $\bar{c} = a^2/b^2$ with a and b defined in eq. (9). Both membrane and flexural stresses are obtained starting from a polynomial expansion in Cartesian coordinates x, y and using Pian's equilibrium filter [48, 50, 58].

3.2. Assumed displacements

The interpolation of the displacement field $\boldsymbol{d}$ is controlled by the 24-component vector $\boldsymbol{d}_e$, which collects the displacements and rotations of the four nodes of the element. The assumed stress approximation satisfies the equilibrium equations for zero distributed loads, and hence

$$\boldsymbol{D}_m^T \boldsymbol{t}_m = \boldsymbol{0} \quad , \quad \boldsymbol{D}_b^T \boldsymbol{t}_b + \boldsymbol{I}_s^T \boldsymbol{t}_s = \boldsymbol{0} \quad , \quad \boldsymbol{D}_s^T \boldsymbol{t}_s = 0 \tag{13}$$

with

$$\boldsymbol{D}_b = \begin{bmatrix} 0 & -\partial/\partial X \\ \partial/\partial Y & 0 \\ \partial/\partial X & -\partial/\partial Y \end{bmatrix} \quad , \quad \boldsymbol{I}_s = \begin{bmatrix} 0 & -1 \\ 1 & 0 \end{bmatrix} \quad , \quad \boldsymbol{D}_s = \begin{bmatrix} \partial/\partial X \\ \partial/\partial Y \end{bmatrix}. \tag{14}$$

the internal work can be obtained by integrating on the element contour. Therefore only contour displacements are needed. The displacement interpolation $\boldsymbol{d}_k$ along element side k is defined as the sum of three contributions

$$\boldsymbol{d}_k[\zeta] = \boldsymbol{d}_{kl}[\zeta] + \boldsymbol{d}_{kq}[\zeta] + \boldsymbol{d}_{kc}[\zeta] \tag{15a}$$

where $-1 \leq \zeta \leq 1$ is a one-dimensional coordinate along element side k. The first term is a linear expansion

$$\boldsymbol{d}_{kl}[\zeta] = \frac{1}{2}[(1-\zeta)\boldsymbol{d}^i + (1+\zeta)\boldsymbol{d}^j], \quad \begin{cases} \boldsymbol{d}^i = [d_x^i,\, d_y^i,\, d_z^i]^T \\ \boldsymbol{d}^j = [d_x^j,\, d_y^j,\, d_z^j]^T \end{cases} \tag{15b}$$

where superscripts i, j denote the nodes of element side k. The second and third terms correspond to quadratic and cubic expansions for the normal component of the element side displacements

$$\boldsymbol{d}_{kq}[\zeta] = \frac{1}{8} L_k(\zeta^2 - 1) \begin{bmatrix} (\varphi_z^i - \varphi_z^j)\, \boldsymbol{n}_k \\ -(\boldsymbol{\varphi}^i - \boldsymbol{\varphi}^j)^T \boldsymbol{n}_k \end{bmatrix}, \quad \boldsymbol{d}_{kc}[\zeta] = \frac{1}{4} L_k(\zeta - \zeta^3) \begin{bmatrix} \boldsymbol{n}_k \\ 0 \end{bmatrix} \theta \tag{15c}$$

with the bending rotations

$$\boldsymbol{\varphi}^i = [\varphi_x^i,\, \varphi_y^i]^T \quad , \quad \boldsymbol{\varphi}^j = [\varphi_x^j,\, \varphi_y^j]^T \tag{15d}$$

and $\boldsymbol{n}_k = [n_{kx}, n_{ky}]^T$ is the normal vector to the element side and L_k is the side length. The angle θ is the average in-plane distortional rotation defined by

$$\theta = \frac{1}{4} \sum_{i=1}^{4} \varphi_z^i - \bar{\varphi}_z \tag{15e}$$

with $\bar{\varphi}_z$ the average in-plane rigid rotation of the element

$$\begin{aligned} &\bar{\varphi}_z = \boldsymbol{N}_\theta \boldsymbol{d}_{me} \\ &\boldsymbol{N}_\theta = \frac{1}{4\Omega_e} \left[-y_4 + y_3,\ x_4 - x_3,\ -y_4 + y_1,\ x_4 - x_1,\ -y_2 + y_1,\ x_2 - x_1,\ -y_3 + y_2,\ x_3 - x_2\right]. \end{aligned} \tag{15f}$$

where $\boldsymbol{d}_{me}$ collects the nodal displacements and rotations describing the membrane behavior and $\{x_i,\, y_i\},\ i = 1, .., 4$ are the nodal coordinates in the local reference frame. By definition, the linear part $\boldsymbol{d}_{kl}$ and the quadratic part $\boldsymbol{d}_{kq}$ are continuous at the inter-element boundaries. The cubic contribution $\boldsymbol{d}_{kc}$ corresponds to an incompatible mode which is added to avoid rank defectiveness [50]. Finally, a simple bilinear interpolation for bending rotations is used along the side

$$\boldsymbol{\varphi}_k[\zeta] = \frac{1}{2}[(1-\zeta)\boldsymbol{\varphi}_i + (1+\zeta)\boldsymbol{\varphi}_j], \quad \boldsymbol{\varphi}_k[\zeta] = [\varphi_x,\, \varphi_y]^T \tag{15g}$$

3.3. Compliance and compatibility

Substituting the assumed stress (12) and assumed displacement (15) fields into equation (2), the mixed strain energy Φ_e of the element is defined as follows

$$\Phi_e = \boldsymbol{\beta}_e^T \boldsymbol{D}_e \boldsymbol{d}_e - \frac{1}{2} \boldsymbol{\beta}_e^T \boldsymbol{H}_e \boldsymbol{\beta}_e \tag{16a}$$

where $\boldsymbol{H}_e$ and $\boldsymbol{D}_e$ are the element compliance matrix and the compatibility matrix respectively. The compliance matrix can be written as follows

$$\boldsymbol{H}_e = \begin{bmatrix} \boldsymbol{H}_m & \boldsymbol{H}_{mb} & \boldsymbol{0} \\ & \boldsymbol{H}_b & \boldsymbol{0} \\ \text{sym} & & \boldsymbol{H}_s \end{bmatrix} \tag{16b}$$

where

$$\boldsymbol{H}_m = \int_{\Omega_e} \left\{ \boldsymbol{B}_m^T \boldsymbol{E}_m^{-1} \boldsymbol{B}_m \right\} \mathrm{d}\Omega, \quad \boldsymbol{H}_{mb} = \int_{\Omega_e} \left\{ \boldsymbol{B}_m^T \boldsymbol{E}_{mb}^{-1} \boldsymbol{B}_b \right\} \mathrm{d}\Omega \tag{16c}$$

and

$$\boldsymbol{H}_b = \int_{\Omega_e} \left\{ \boldsymbol{B}_b^T \boldsymbol{E}_b^{-1} \boldsymbol{B}_b \right\} \mathrm{d}\Omega, \quad \boldsymbol{H}_s = \int_{\Omega_e} \left\{ \boldsymbol{B}_s^T \boldsymbol{E}_s^{-1} \boldsymbol{B}_s \right\} \mathrm{d}\Omega. \tag{16d}$$

The integrations are performed assuming $\boldsymbol{E}_m$, $\boldsymbol{E}_{mb}$, $\boldsymbol{E}_b$ and $\boldsymbol{E}_s$ are constant over the element domain Ω_e. As the compatibility matrix is based on a self-equilibrated stress interpolation, and it is evaluated through analytical contour integration, it can be written ain the following form

$$\boldsymbol{D}_e = \begin{bmatrix} \boldsymbol{D}_m & \boldsymbol{0} \\ \boldsymbol{0} & \boldsymbol{D}_f \end{bmatrix}, \quad \boldsymbol{D}_m = \sum_{k=1}^{4} \boldsymbol{D}_{mk} + \boldsymbol{D}_c \ , \quad \boldsymbol{D}_f = \sum_{k=1}^{4} \boldsymbol{D}_{fk} \tag{16e}$$

where the matrices $\boldsymbol{D}_{mk}$ and $\boldsymbol{D}_{fk}$ are defined by

$$\begin{aligned} \boldsymbol{\beta}_m^T \boldsymbol{D}_{mk} \boldsymbol{d}_{em} &= \int_{-1}^{1} \boldsymbol{t}_m^T[\zeta] \boldsymbol{N}_{mk}^T \boldsymbol{d}_{mk}[\zeta] \, \mathrm{d}\zeta \\ \boldsymbol{\beta}_m^T \boldsymbol{D}_c \boldsymbol{d}_{em} &= \int_{-1}^{1} \boldsymbol{t}_m^T[\zeta] \boldsymbol{N}_{mk}^T \boldsymbol{d}_c[\zeta] \, \mathrm{d}\zeta \\ \boldsymbol{\beta}_f^T \boldsymbol{D}_{fk} \boldsymbol{d}_{ef} &= \int_{-1}^{1} \boldsymbol{t}_f^T[\zeta] \boldsymbol{N}_{fk}^T \boldsymbol{d}_{fk}[\zeta] \, \mathrm{d}\zeta \end{aligned} \tag{16f}$$

and the vectors $\boldsymbol{d}_{em}$ and $\boldsymbol{d}_{ef}$ collect the nodal displacements and rotations describing the membrane and flexural behavior, respectively. Finally, the matrices $\boldsymbol{N}_{mk}, \boldsymbol{N}_{fk}$ split the components of the normal to the element side, i.e.

$$\boldsymbol{N}_{mk} = \begin{bmatrix} n_{kx} & 0 & n_{ky} \\ 0 & n_{ky} & n_{kx} \end{bmatrix}, \quad \boldsymbol{N}_{fk} = \begin{bmatrix} 0 & 0 & 0 & n_{kx} & n_{ky} \\ n_{kx} & n_{ky} & 0 & 0 & 0 \\ -n_{ky} & 0 & -n_{kx} & 0 & 0 \end{bmatrix}. \tag{16g}$$

3.4. Geometrical stiffness matrix

A linear finite element can be made geometrically nonlinear using corotational algebra to describe the rigid body motion [15]. With respect to the fixed frame $\{\boldsymbol{e}_1, \boldsymbol{e}_2, \boldsymbol{e}_3\}$, a corotational (CR) frame $\{\bar{\boldsymbol{e}}_1, \bar{\boldsymbol{e}}_2, \bar{\boldsymbol{e}}_3\}$ is defined as

$$\bar{\boldsymbol{e}}_k = \boldsymbol{Q}[\boldsymbol{\alpha}] \boldsymbol{e}_k, \quad k = 1 \ldots 3 \tag{17}$$

with $\boldsymbol{Q}$ being a rigid rotation, parametrized by the rotation vector $\boldsymbol{\alpha}$ according to Rodrigues' formulation [59]. The origin is assumed to be translated by vector $\boldsymbol{c}$. Denoting the displacement and rotation associated with position $\boldsymbol{X}$ in the fixed reference frame by $\boldsymbol{d}$ and $\boldsymbol{R}$, respectively, the following geometrical relationships hold

$$\bar{\boldsymbol{d}} = \boldsymbol{Q}^T (\boldsymbol{X} + \boldsymbol{d} - \boldsymbol{c}) - \boldsymbol{X} \quad , \quad \bar{\boldsymbol{R}} = \boldsymbol{Q}^T \boldsymbol{R} \tag{18}$$

with $\bar{\boldsymbol{d}}$ and $\bar{\boldsymbol{R}}$ being the displacement and the rotation in the corotational frame. Using a vector parametrization for $\bar{\boldsymbol{R}}$ and $\boldsymbol{R}$ and denoting by $\bar{\boldsymbol{\psi}}$ and $\boldsymbol{\psi}$ the rotation vectors, we have

$$\bar{\boldsymbol{\psi}} = \log(\bar{\boldsymbol{R}}[\bar{\boldsymbol{\psi}}]) = \log\left(\boldsymbol{Q}^T[\boldsymbol{\alpha}]\boldsymbol{R}[\boldsymbol{\psi}]\right). \tag{19}$$

A CR frame can be defined for each element through the element rotation vector $\boldsymbol{\alpha}_e$ which is a function of the element kinematical parameters $\boldsymbol{d}_e$ in the fixed frame

$$\boldsymbol{\alpha}_e = \boldsymbol{\alpha}_e[\boldsymbol{d}_e]. \tag{20}$$

The local kinematical parameters $\bar{\boldsymbol{d}}_e$ in the CR frame are related to $\boldsymbol{d}_e$ by the geometrical transformation

$$\bar{\boldsymbol{d}}_e = \boldsymbol{g}[\boldsymbol{d}_e] \tag{21}$$

where $\boldsymbol{g}$ collects the CR transformations for displacements (18) and rotations (19) opportunely rearranged once the definition of local kinematical parameters $\bar{\boldsymbol{d}}_e$ of the finite element is fixed.

Based on the above relations, the linear finite element characterized by the mixed energy expression (16a) can be transformed into a geometrically nonlinear element simply by introducing a corotational description and assuming that the element kinematical parameters in eq. (16a) are referred to the corotational frame. This leads to:

$$\Phi_e[\boldsymbol{t}_e, \boldsymbol{d}_e] = \boldsymbol{t}_e^T \boldsymbol{D}_e \boldsymbol{g}[\boldsymbol{d}_e] - \frac{1}{2}\boldsymbol{t}_e^T \boldsymbol{H}_e \boldsymbol{t}_e. \tag{22}$$

The element energy can be expressed in terms of the element vector

$$\boldsymbol{u}_e = \{\boldsymbol{t}_e,\ \boldsymbol{d}_e\}^T \tag{23}$$

which collects all the parameters defining the element state in a single vector and can be related to the global configuration vector $\boldsymbol{u}$ through the standard finite element stiffness matrix assembly procedure [60]

$$\boldsymbol{u}_e = \boldsymbol{A}_e \boldsymbol{u} \tag{24}$$

where matrix $\boldsymbol{A}_e$ implicitly contains the assembly constraints between elements. For the Hellinger-Reissner formulation used here, the components of $\boldsymbol{u}$ are the global displacements/rotations of the nodes of the elements and the the stress parameters of each element. Note that the stress parameters can be solved at the element level, and then a pseudo-compatible scheme can be employed [57].

3.4.1. Taylor's expansion of corotational kineamtics

The corotational approach is a convenient tool to express the strain energy variations, because the nonlinearity is limited to the geometrical relationship $\boldsymbol{g}[\boldsymbol{d}_e]$, eq. (21). The Taylor expansion of this relationship can be written as

$$\boldsymbol{g}[\boldsymbol{d}_e] = \boldsymbol{g}_1[\boldsymbol{d}_e] + \frac{1}{2}\boldsymbol{g}_2[\boldsymbol{d}_e, \boldsymbol{d}_e] + \frac{1}{6}\boldsymbol{g}_3[\boldsymbol{d}_e, \boldsymbol{d}_e, \boldsymbol{d}_e] + \frac{1}{24}\boldsymbol{g}_4[\boldsymbol{d}_e, \boldsymbol{d}_e, \boldsymbol{d}_e, \boldsymbol{d}_e] + \cdots \tag{25}$$

where $\boldsymbol{g}_n$ are n-multilinear symmetric forms which express the nth Fréchet derivative of the function $\boldsymbol{g}[\boldsymbol{d}_e]$. In the following, vector $\boldsymbol{u}_i$ ($i = 1 \ldots 4$) denotes a generic variation of the global finite element state vector, and vector $\boldsymbol{u}_{ei} = \boldsymbol{A}_e \boldsymbol{u}_i = \{\boldsymbol{t}_{ei}, \boldsymbol{d}_{ei}\}^T$ the corresponding vector at the element level that collects stress and displacement parameters. With the same notation $\boldsymbol{u}_0$ and $\boldsymbol{u}_{e0}$ are the global and element reference configuration vectors.

3.4.2. Second-order energy variations

Second-order energy variations are used in the evaluation of the fundamental mode and the buckling modes. In both cases using eq. (25) and the energy expression (22), the contribution of the element to the energy variation is expressed as

$$\Phi_e^{''}\boldsymbol{u}_{e1}\boldsymbol{u}_{e2} = \boldsymbol{t}_{e1}^T\boldsymbol{D}_e\boldsymbol{g}_1[\boldsymbol{d}_{e2}] + \boldsymbol{t}_{e2}^T\boldsymbol{D}_e\boldsymbol{g}_1[\boldsymbol{d}_{e1}] - \boldsymbol{t}_{e1}^T\boldsymbol{H}_e\boldsymbol{t}_{e2} + \boldsymbol{t}_{e0}^T\boldsymbol{D}_e\boldsymbol{g}_2[\boldsymbol{d}_{e1},\boldsymbol{d}_{e2}]. \tag{26}$$

Introducing matrices $\boldsymbol{L}_1$ and $\boldsymbol{G}[\boldsymbol{t}_e]$ through the following equivalences

$$\boldsymbol{L}_1\boldsymbol{d}_{ej} = \boldsymbol{g}_1[\boldsymbol{d}_{ej}] \quad , \quad \boldsymbol{d}_{e1}^T\boldsymbol{G}[\boldsymbol{t}_{e0}]\boldsymbol{d}_{e2} = \boldsymbol{t}_{e0}^T\boldsymbol{D}_e\boldsymbol{g}_2[\boldsymbol{d}_{e1},\boldsymbol{d}_{e2}], \tag{27}$$

eq. (26) can be rearranged in a more compact form:

$$\boldsymbol{u}_{e1}^T\Phi_e^{''}\boldsymbol{u}_{e2} = \boldsymbol{u}_{e1}^T\boldsymbol{K}_e\boldsymbol{u}_{e2} \quad , \quad \boldsymbol{K}_e = \begin{bmatrix} -\boldsymbol{H}_e & \boldsymbol{D}_e\boldsymbol{L}_1 \\ \boldsymbol{L}_1^T\boldsymbol{D}_e^T & \boldsymbol{G}[\boldsymbol{t}_{e0}] \end{bmatrix}. \tag{28}$$

The mixed tangential stiffness matrix of the element $\boldsymbol{K}_e$ can be used directly through a standard assemblage process to obtain the overall stiffness matrix $\boldsymbol{K}$

$$\boldsymbol{u}_1^T\Phi^{''}\boldsymbol{u}_2 = \boldsymbol{u}_1^T\boldsymbol{K}\boldsymbol{u}_2 \quad , \quad \boldsymbol{K} = \sum_e \boldsymbol{A}_e^T\boldsymbol{K}_e\boldsymbol{A}_e. \tag{29}$$

4. NUMERICAL RESULTS

The performance of the proposed shell element is tested for the linear static and buckling analyses of VAT plates with different boundary conditions and loading conditions. In particular, two distinct in-plane boundary/load conditions are considered to validate the in-plane and buckling behaviors (see Fig. 2), and a simply supported plate under constant pressure is tested to check the out-plane behavior. The length of the square plate is $l = 1.0\ m$ and the thickness of each lamina is $t = 1.272 \cdot 10^{-4}\ m$. The material properties of the plate are tabulated in Table 1 and the layer stacking sequences (LSS) are cited in Table 2. The local fibre orientation $\theta(X)$ within a VAT lamina is given by the notation

$$\theta(X) = \phi + \frac{2\,(T_1 - T_0)}{L_x}|X| + T_0$$

where ϕ is the rotation of the fibre paths with respect to the global X-axis, T_0 is the fiber orientation angle at the plate center ($X = 0$) with respect to ϕ, and T_1 is the fiber orientation angle at the plate ends ($X = \pm L_x/2$) with respect to ϕ. The distribution of $\theta(x)$ over the planform is depicted graphically in Fig. (3) for the first lamina of the VAT plate with LSS $(45 \pm \langle 90|0\rangle)_{3s}$.

For the linear static analysis the recovery of the in-plane and out-plane stresses are used as test metrics for validation in terms of overall solution over the domain and point-wise convergence. For the buckling analysis the convergence of buckling loads and modes is presented. To validate the present MISS-4 element comparisons have been made with the S4R shell element of the finite element code ABAQUS and with numerical solutions obtained from differential quadrature method (DQM). Details regarding the use of the DQM are explained in the following.

4.1. Differential quadrature method: fundamentals equation

Differential quadrature (DQ) is a numerical discretisation technique proposed by Bellman et al. [61] that approximates the partial derivative of a functional field with respect to a specific spatial variable using a

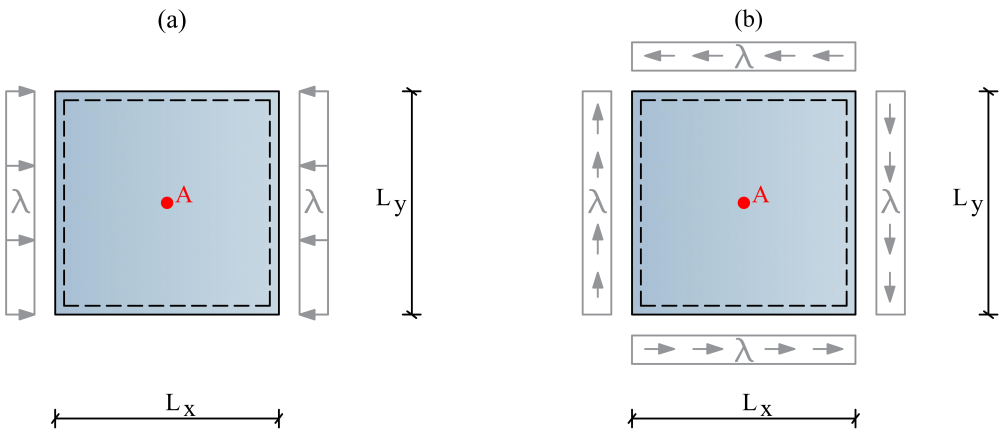

Figure 2: Geometry, boundary conditions and loads for the plate with the in-plane behavior. The test denoted with (a) and (b) correspond to Test 1 and Test 2 in the following.

E_1	E_2	ν_{12}	G_{12}	G_{13}	G_{23}
$[GPa]$	$[GPa]$	$[-]$	$[GPa]$	$[GPa]$	$[GPa]$
181.00	10.27	0.28	7.17	4.00	4.00

Table 1: Material properties.

linear weighted sum of all the functional values in the domain. For example, the n^{th} partial derivative of function $f(x)$ at the i^{th} discretisation point is

$$\frac{\partial^n f(x_i)}{\partial x^n} = A_{ij}^{(n)} f(x_j), \quad i = 1, 2, \ldots, N_p \tag{30}$$

where x_i is the set of N_p discretisation points in the x-direction, typically defined by the non-uniform Gauss-Lobatto-Chebychev distribution, $A_{ij}^{(n)}$ are the weighting coefficients of the n^{th} derivative, and repeated index j means summation from 1 to N_p. The same technique is easily extended to the remaining two spatial dimensions to compute mixed derivatives.

The key to applying DQ is finding the value of the weighting coefficients for any order derivative and number of grid points. In this regard, Shu and Richard [62] proposed the Generalised Differential Quadrature (GDQ), whereby Lagrange polynomials are used as the underlying polynomial basis for deriving $A_{ij}^{(n)}$. The interpolation coefficient matrix g_k for the Lagrangian polynomial basis [63] is given by

$$g_k(x) = \frac{m(x)}{(x - x_k)m^{(1)}(x_k)}, \quad k = 1, 2, \ldots, N_p \tag{31}$$

Plate	Layer arrangements
LSS1	$(0 \pm \langle 45 \vert 0 \rangle)_{3s}$
LSS2	$(45 \pm \langle 90 \vert 0 \rangle)_{3s}$
LSS3	$(90 \pm \langle 0 \vert 45 \rangle)_{3s}$

Table 2: Lamina orientations.

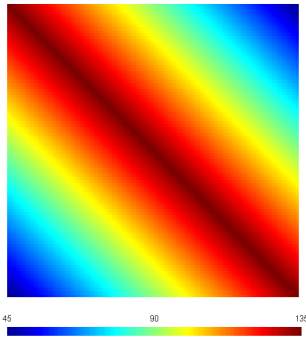

Figure 3: Distibution of $\theta(X)$ for the first lamina of the VAT plate $(45 \pm \langle 90|0\rangle)_{3s}$.

where

$$m(x) = \prod_{j=1}^{N_p}(x - x_j) \quad \text{and} \quad m^{(1)}(x_i) = \prod_{k=1,k\neq i}^{N_p}(x_i - x_k) \tag{32}$$

and this leads to the weighting coefficients of the derivatives $A_{ij}^{(n)}$,

$$A_{ij}^{(1)} = \frac{1}{x_j - x_i}\prod_{k=1,k\neq i,j}^{N_p}\frac{x_i - x_k}{x_j - x_k} \quad \text{for} \quad i \neq j \quad \text{and} \quad A_{ii}^{(1)} = \sum_{k=1,k\neq i}^{N_p}\frac{1}{x_i - x_k}. \tag{33}$$

Subsequently, all higher-order weighting coefficients are obtained by direct matrix multiplication, i.e. $[A^{(m)}] = [A^{(1)}][A^{(m-1)}]$, with $m = 2, 3, \ldots, N_p - 1$ [64]. In this manner, any set of linear differential equations can be written as a linear system of algebraic equations by replacing the differential operators with the weighting matrix in eq. (30). Thus, the unknown functional values $f(x_i)$ at each grid point are found by solving the strong form of the system of equations with pertinent essential or natural boundary conditions imposed on the boundary points.

4.2. Plate element for DQM

To model the buckling behavior of VAT panels the classic equilibrium equations of a flat plate subjected to in-plane and transverse loading are used. The classical Kirchhoff assumptions of mid-plane normals remaining normal and unextended, and plane sections remaining plane are invoked. Thus, transverse shear strains and transverse normal strains are deemed negligible compared to their in-plane counterparts. Furthermore, Lagrangian linear kinematics with von Kármán nonlinear strains are employed. Therefore,

$$\begin{cases} \dfrac{\partial N_x}{\partial X} + \dfrac{\partial N_{xy}}{\partial Y} = 0 \\ \dfrac{\partial N_y}{\partial Y} + \dfrac{\partial N_{xy}}{\partial X} = 0 \\ \dfrac{\partial^2 M_x}{\partial^2 X} + \dfrac{\partial^2 M_{xy}}{\partial X \partial Y} + \dfrac{\partial^2 M_y}{\partial^2 Y} + N_x\dfrac{\partial^2 d_z}{\partial^2 X} + 2N_{xy}\dfrac{\partial^2 d_z}{\partial X \partial Y} + N_y\dfrac{\partial^2 d_z}{\partial^2 Y} + p_z = 0 \end{cases} \tag{34}$$

where the nonlinear part of the third governing equation (34) represents the transverse components of the membrane forces that arise once the panel has buckled. Finally, p_z is the distributed load in the Z direction.

The membrane forces ($\boldsymbol{t}_m$) and bending moments ($\boldsymbol{t}_b$) per unit width in equation (34) are defined by

$$\boldsymbol{t}_m = \boldsymbol{E}_m(X, Y) \cdot (\boldsymbol{e} + \boldsymbol{\eta}) + \boldsymbol{E}_{mb}(X, Y) \cdot \boldsymbol{\chi} \qquad \boldsymbol{t}_b = \boldsymbol{E}_{mb}(X, Y) \cdot (\boldsymbol{e} + \boldsymbol{\eta}) + \boldsymbol{E}_b(X, Y) \cdot \boldsymbol{\chi} \tag{35}$$

where $\boldsymbol{E}_m(X,Y)$, $\boldsymbol{E}_{mb}(X,Y)$ and $\boldsymbol{E}_b(X,Y)$ are the membrane, coupling and bending stiffness matrices of the Classical Laminate Analysis as introduced previously in eq. (5). Note that due to the variable stiffness design of the panel these terms are functions of location (X,Y). Finally, the linear and nonlinear membranes strains, $\boldsymbol{e}$ and $\boldsymbol{\eta}$, and curvatures $\boldsymbol{\chi}$ of the reference surface are given by.

$$\boldsymbol{e} = \begin{bmatrix} \partial d_x/\partial X \\ \partial d_y/\partial Y \\ \partial d_y/\partial X + \partial d_x/\partial Y \end{bmatrix}, \quad \boldsymbol{\eta} = \begin{bmatrix} 1/2\,(\partial d_z/\partial X)^2 \\ 1/2\,(\partial d_z/\partial Y)^2 \\ (\partial d_z/\partial X)(\partial d_z/\partial Y) \end{bmatrix}, \quad \boldsymbol{\chi} = -\begin{bmatrix} \partial^2 d_z/\partial^2 X \\ \partial^2 d_z/\partial^2 Y \\ 2\,\partial^2 d_z/\partial X \partial Y \end{bmatrix} \tag{36}$$

where d_z, d_y, d_z are the deflections of the plate reference surface in the Cartesian X, Y, Z-coordinates, respectively.

Finally, the essential and natural boundary conditions that need to be applied to fully constrain the boundary value problem are

$$\begin{cases} d_n = \hat{d}_n & \text{or} \quad N_{nn} = \hat{N}_{nn} \\ d_s = \hat{d}_s & \text{or} \quad N_{ns} = \hat{N}_{ns} \\ d_z = \hat{d}_z & \text{or} \quad Q_{nz} + \dfrac{\partial M_{ns}}{\partial s} = \hat{Q}_{nz} + \dfrac{\partial \hat{M}_{ns}}{\partial s} \\ \dfrac{\partial d_z}{\partial n} = \dfrac{\partial \hat{d}_z}{\partial n} & \text{or} \quad M_{nn} = \hat{M}_{nn} \end{cases} \tag{37}$$

where

$$\begin{aligned} d_n &= u_x n_x + u_y n_y & u_s &= -u_x n_y + n_x u_y \\ \frac{\partial}{\partial n} &= n_x \frac{\partial}{\partial x} + n_y \frac{\partial}{\partial y} & \frac{\partial}{\partial s} &= -n_y \frac{\partial}{\partial x} + n_x \frac{\partial}{\partial y} \\ N_{nn} &= N_x n_x^2 + 2N_{xy} n_x n_y + N_y n_y^2 & N_{ns} &= \left(N_y - N_x\right) n_x n_y + N_{xy}\left(n_x^2 - n_y^2\right) \\ Q_{nz} &= \frac{\partial M_x}{\partial X} n_x + \frac{\partial M_{xy}}{\partial Y} n_x + \frac{\partial M_y}{\partial Y} n_y + \frac{\partial M_{xy}}{\partial X} n_y + \left(N_x \frac{\partial d_z}{\partial X} + N_{xy} \frac{\partial d_z}{\partial Y}\right) n_x + \left(N_{xy} \frac{\partial d_z}{\partial X} + N_y \frac{\partial d_z}{\partial Y}\right) n_y \\ M_{nn} &= M_x n_x^2 + 2M_{xy} n_x n_y + M_y n_y^2 & M_{ns} &= \left(M_y - M_x\right) n_x n_y + M_{xy}\left(n_x^2 - n_y^2\right) \end{aligned}$$

and the directional terms are defined by $n_x = \cos\upsilon$ and $n_y = \sin\upsilon$ where υ is the angle between the normal to the boundary and the global X-axis, and prescribed quantities on the boundary are denoted by a superimposed hat $\hat{}$.

By linearising the pre-buckling path, i.e. assuming that displacement gradients of the elastic solution remain small such that the rotations of the reference surface $(d^e_{z,x}, d^e_{z,y}) \ll 1$, and therefore are negligible, a generalised eigenvalue problem in terms of the displacement unknowns $\boldsymbol{d} = (\boldsymbol{d}_x, \boldsymbol{d}_y, \boldsymbol{d}_z)$ at the DQ grid points is derived. Hence, substituting the weighting matrix of eq. (30) for the differential operators into equation (34), an algebraic system of equations is derived

$$\begin{bmatrix} \boldsymbol{A}_x & \boldsymbol{0} & \boldsymbol{A}_y & \boldsymbol{0} & \boldsymbol{0} & \boldsymbol{0} \\ \boldsymbol{0} & \boldsymbol{A}_y & \boldsymbol{A}_x & \boldsymbol{0} & \boldsymbol{0} & \boldsymbol{0} \\ \boldsymbol{0} & \boldsymbol{0} & \boldsymbol{0} & \boldsymbol{A}_{xx} & \boldsymbol{A}_{yy} & 2\boldsymbol{A}_{xy} \end{bmatrix} \begin{bmatrix} \boldsymbol{N}_x \\ \boldsymbol{N}_y \\ \boldsymbol{N}_{xy} \\ \boldsymbol{M}_x \\ \boldsymbol{M}_y \\ \boldsymbol{M}_{xy} \end{bmatrix} + \lambda \begin{bmatrix} \boldsymbol{N}^e_x & \boldsymbol{N}^e_y & 2\boldsymbol{N}^e_{xy} \end{bmatrix} \begin{bmatrix} \boldsymbol{A}_{xx} \\ \boldsymbol{A}_{yy} \\ \boldsymbol{A}_{xy} \end{bmatrix} \boldsymbol{d}_z = \boldsymbol{0} \tag{38}$$

where $(\boldsymbol{N}_x^e, \boldsymbol{N}_y^e, \boldsymbol{N}_{xy}^e)$ are the membrane forces acting on the reference surface calculated for a prescribed unit loading in the linearised pre-buckling problem, and λ is a load proportionality factor. In DQ form the membrane force and bending moments are calculated as follows

$$\begin{bmatrix} \boldsymbol{N}_x \\ \boldsymbol{N}_y \\ \boldsymbol{N}_{xy} \end{bmatrix} = \boldsymbol{E}_m \begin{bmatrix} \boldsymbol{A}_x & \boldsymbol{0} \\ \boldsymbol{0} & \boldsymbol{A}_y \\ \boldsymbol{A}_y & \boldsymbol{A}_x \end{bmatrix} \begin{bmatrix} \boldsymbol{d}_x \\ \boldsymbol{d}_y \end{bmatrix} + \boldsymbol{E}_{mb} \begin{bmatrix} -\boldsymbol{A}_{xx} \\ -\boldsymbol{A}_{yy} \\ -2\boldsymbol{A}_{xy} \end{bmatrix} \boldsymbol{d}_z \tag{39}$$

$$\begin{bmatrix} \boldsymbol{M}_x \\ \boldsymbol{M}_y \\ \boldsymbol{M}_{xy} \end{bmatrix} = \boldsymbol{E}_{mb} \begin{bmatrix} \boldsymbol{A}_x & \boldsymbol{0} \\ \boldsymbol{0} & \boldsymbol{A}_y \\ \boldsymbol{A}_x & \boldsymbol{A}_y \end{bmatrix} \begin{bmatrix} \boldsymbol{d}_x \\ \boldsymbol{d}_y \end{bmatrix} + \boldsymbol{E}_b \begin{bmatrix} -\boldsymbol{A}_{xx} \\ -\boldsymbol{A}_{yy} \\ -2\boldsymbol{A}_{xy} \end{bmatrix} \boldsymbol{d}_z \tag{40}$$

where $\boldsymbol{A}_x, \boldsymbol{A}_y, \boldsymbol{A}_{xx}, \boldsymbol{A}_{yy}, \boldsymbol{A}_{xy}$ are the first-order and second-order DQ weighting matrices, and $\boldsymbol{d}_x, \boldsymbol{d}_y, \boldsymbol{d}_z$ are the vectors of unknowns at the DQ grid points. Thus, we need to solve the generalised eigenvalue problem

$$\left(\boldsymbol{K}_0 + \lambda \boldsymbol{K}_g^e\right) \boldsymbol{d} = \boldsymbol{0} \tag{41}$$

where the displacement unknowns at the DQ gridpoints have been combined into one vector $\boldsymbol{d} = (\boldsymbol{d}_x, \boldsymbol{d}_y, \boldsymbol{d}_z)$, $\boldsymbol{K}_0$ is the linearised stiffness matrix and $\boldsymbol{K}_g^e$ the geometric stiffness matrix evaluated for the prescribed unit loading in the pre-buckling step. To find the pre-buckling values of $(\boldsymbol{N}_x^e, \boldsymbol{N}_y^e, \boldsymbol{N}_{xy}^e)$ from pre-buckling displacements, the elastic displacement vector $\boldsymbol{d}^e = (\boldsymbol{d}_x^e, \boldsymbol{d}_y^e, \boldsymbol{d}_z^e)$ is determined by solving the governing equations $\boldsymbol{K}_0 \boldsymbol{d}^e = \boldsymbol{f}_{ext}$ with the appropriate essential (displacement) and natural (stress) boundary conditions reflected in the external forcing vector $\boldsymbol{f}_{ext}$. Once $\boldsymbol{K}_g^e$ is determined from the pre-buckling values of $(\boldsymbol{N}_x^e, \boldsymbol{N}_y^e, \boldsymbol{N}_{xy}^e)$, the eigenvalues (buckling loads) and eigenvectors (buckling modes) are calculated from the generalised eigenvalue problem. For more details regarding the numerical implementation of the DQM solver, the interested reader is directed to [26].

4.3. Linear static analysis

In the following three results for the three validation tests outlined above are discussed. The first regards the plate under mono-axial compression. The results for different mesh densities for the three LSS are shown in Table 3 and in Fig. (4) for MISS-4 and DQM. The results highlight the good performance of the MISS-4 element in terms of the error for rough meshes and the rate of convergence. Overall the performance is comparable to DQM and also correlates closely with the S4R element in Abaqus.

Similar obersvations can be made regarding the second load case under in-plane shear loading. For this test convergence results are reported in Table 4 and in Fig. (5) for the LSS $(90 \pm \langle 0|45 \rangle)_{3s}$. Also in this case the good rate convergence of MISS-4 can be observed.

The results for the out-plane bending behavior are reported in Table 5 and in Figs. (6) and (7). Some small differences between the converged DQM and MISS-4 results can be observed, and the likely reason for this is the MISS-4 element accounts for first-order shear effects whereas the DQM model does not. The rate of convergence is of the order of the element length square, i.e. h^2, and the overall performance between DQM and MISS-4 are comparable.

Test 1		Mesh/Grid	N_x	N_y	N_{xy}
$(0 \pm \langle 45\|0\rangle)_{3s}$	MISS-4	8·8	-1.113	-0.231	0.000
		16·16	-1.130	-0.292	0.000
		32·32	-1.135	-0.322	0.000
		64·64	-1.136	-0.336	0.000
		100·100	-1.136	-0.341	0.000
	DQM	10 ·10	-1.128	-0.252	0.000
		18·18	-1.134	-0.300	0.000
		26·26	-1.135	-0.316	0.000
		34·34	-1.135	-0.324	0.000
		42·42	-1.136	-0.329	0.000
	S4R	100·100	-1.136	-0.341	0.000
$(45 \pm \langle 90\|0\rangle)_{3s}$	MISS-4	8·8	-0.939	0.130	-0.143
		16·16	-0.874	0.152	-0.177
		32·32	-0.855	0.154	-0.186
		64·64	-0.849	0.153	-0.188
		100·100	-0.848	0.153	-0.189
	DQM	10 ·10	-0.827	0.183	-0.203
		18·18	-0.846	0.154	-0.190
		26·26	-0.847	0.153	-0.189
		34·34	-0.848	0.153	-0.187
		42·42	-0.848	0.153	-0.189
	S4R	100·100	-0.848	0.152	-0.188
$(90 \pm \langle 0\|45\rangle)_{3s}$	MISS-4	8·8	-0.792	0.124	0.000
		16·16	-0.783	0.141	0.000
		32·32	-0.781	0.146	0.000
		64·64	-0.780	0.147	0.000
		100·100	-0.780	0.147	0.000
	DQM	10 ·10	-0.775	0.144	0.000
		18·18	-0.779	0.148	0.000
		26·26	-0.780	0.147	0.000
		34·34	-0.780	0.147	0.000
		42·42	-0.780	0.147	0.000
	S4R	(100·100)	-0.780	0.147	0.000

Table 3: Test 1: Stress resultants at the midpoint of the VAT plates: $(0 \pm \langle 45|0\rangle)_{3s}$, $(45 \pm \langle 90|0\rangle)_{3s}$ $(90 \pm \langle 0|45\rangle)_{3s}$ subjected to unit axial compression and simply supported boundary conditions

Test 2		Mesh/Grid	N_x	N_y	N_{xy}
$(0 \pm \langle 45\|0\rangle)_{3s}$	MISS-4	8·8	0.000	0.000	-0.993
		16·16	0.000	0.000	-0.998
		32·32	0.000	0.000	-1.000
		64·64	0.000	0.000	-1.000
		100·100	0.000	0.000	-1.000
	DQM	10·10	0.000	0.000	-1.000
		18·18	0.000	0.000	-1.000
		26·26	0.000	0.000	-1.000
		34·34	0.000	0.000	-1.000
		42·42	0.000	0.000	-1.000
	S4R	100·100	0.000	0.000	-1.000
$(45 \pm \langle 90\|0\rangle)_{3s}$	MISS-4	8·8	0.531	0.531	-1.215
		16·16	0.583	0.583	-1.245
		32·32	0.585	0.585	-1.245
		64·64	0.586	0.586	-1.239
		100·100	0.586	0.586	-1.232
	DQM	10·10	0.480	0.480	-1.161
		18·18	0.559	0.559	-1.212
		26·26	0.579	0.579	-1.228
		34·34	0.585	0.585	-1.231
		42·42	0.586	0.586	-1.232
	S4R	100·100	0.586	0.586	-1.232
$(90 \pm \langle 0\|45\rangle)_{3s}$	MISS-4	8·8	0.000	0.000	-1.018
		16·16	0.000	0.000	-1.009
		32·32	0.000	0.000	-1.000
		64·64	0.000	0.000	-1.000
		100·100	0.000	0.000	-1.000
	DQM	10·10	0.000	0.000	-1.000
		18·18	0.000	0.000	-1.000
		26·26	0.000	0.000	-1.000
		34·34	0.000	0.000	-1.000
		42·42	0.000	0.000	-1.000
	S4R	100·100	0.000	0.000	-1.000

Table 4: Test 2: Stress resultants t_m at midpoint for the VAT plates: $(0 \pm \langle 45|0\rangle)_{3s}$, $(45 \pm \langle 90|0\rangle)_{3s}$ $(90 \pm \langle 0|45\rangle)_{3s}$ subjected to unit in-plane shear loading and simply supported boundary conditions.

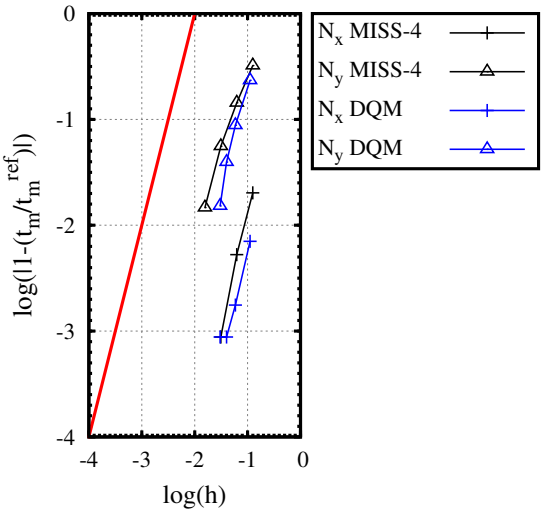

(a) $(0 \pm \langle 45|0\rangle)_{3s}$

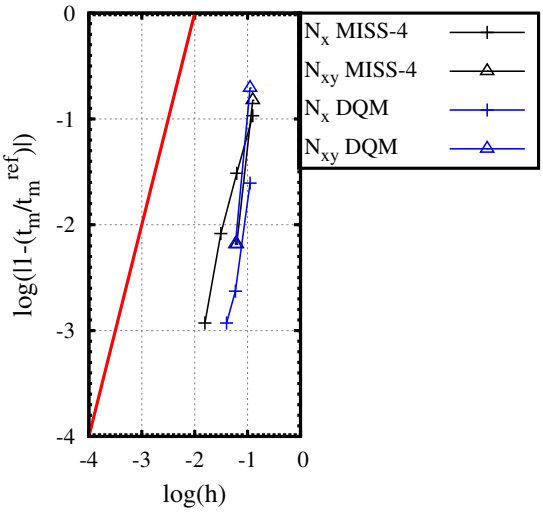

(b) $(45 \pm \langle 90|0\rangle)_{3s}$

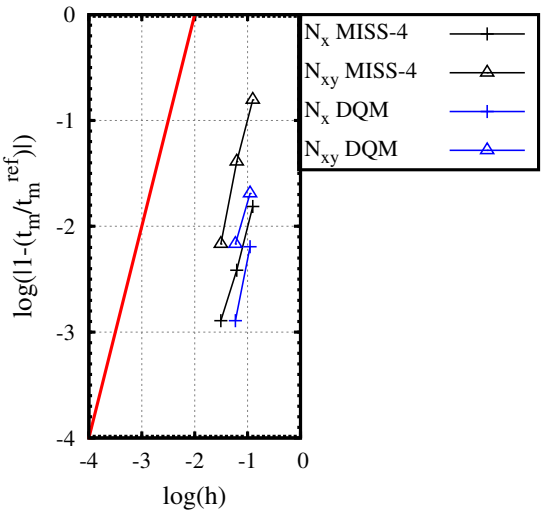

(c) $(90 \pm \langle 45|0\rangle)_{3s}$

Figure 4: Test 1: Convergence of stress resultants t_m at the midpoint of the VAT plates $(0 \pm \langle 45|0\rangle)_{3s}$, $(45 \pm \langle 90|0\rangle)_{3s}$ and $(90 \pm \langle 0|45\rangle)_{3s}$ subjected to unit axial compression and simply supported boundary conditions. t_m^{ref} is the reference value obtained using very fine mesh/grid. h is the characterictic dimension of the mesh/grid and the red line represents h^2 convergence which is shown for reference.

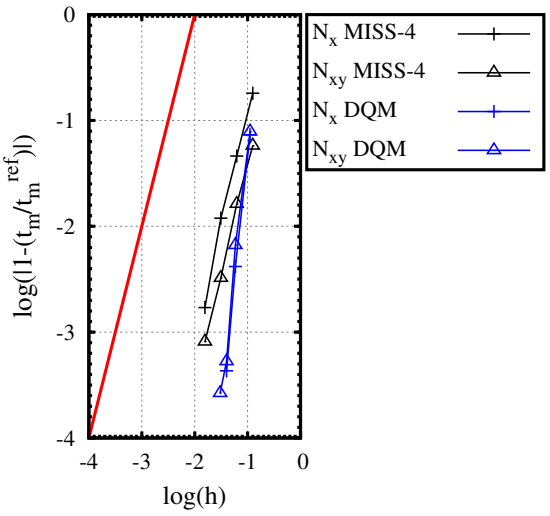

(a) $(45 \pm \langle 90|0 \rangle)_{3s}$

Figure 5: Test 2: Convergence of stress resultants at the midpoint of the VAT plate $(90 \pm \langle 0|45 \rangle)_{3s}$ subjected to unit in-plane shear loading and simply supported boundary conditions. t_m^{ref} is the reference value obtained using very fine mesh/grid. h is the characterstic dimension of the mesh/grid and the red line represents h^2 convergence which is shown for reference.

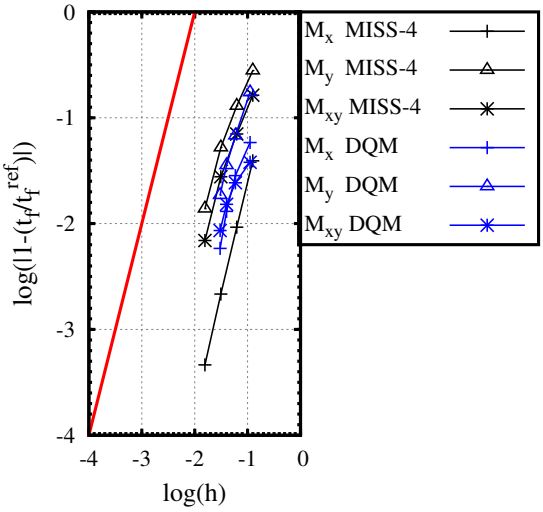

Figure 6: Test 3: Convergence of stress resultants t_f at the midpoint of the VAT plate $(0 \pm \langle 45|0 \rangle)_{3s}$ subjected to a unit pressure loading on the top surface and simply supported boundary conditions. t_f^{ref} is the reference value obtained using very fine mesh/grid. h is the characteristic dimension of the mesh/grid and the red line represents h^2 convergence which is shown for reference.

Test 3		Mesh/Grid	M_x	M_y	M_{xy}	d_z
$(0 \pm \langle 45\|0\rangle)_{3s}$	MISS-4	8·8	-0.0623	-0.0432	-0.0085	-0.000184
		16·16	-0.0642	-0.0522	-0.0094	-0.000204
		32·32	-0.0647	-0.0569	-0.0098	-0.000209
		64·64	-0.0648	-0.0592	-0.0100	-0.000210
		100·100	-0.0648	-0.0600	-0.0101	-0.000210
	DQM	10 ·10	-0.0690	-0.0486	-0.0096	-0.000217
		18·18	-0.0670	-0.0548	-0.0097	-0.000216
		26·26	-0.0660	-0.0567	-0.0098	-0.000214
		34·34	-0.0655	-0.0577	-0.0099	-0.000212
		42·42	-0.0652	-0.0588	-0.0100	-0.000212
	S4R	100·100	-0.0649	-0.0600	-0.0101	-0.000212
$(45 \pm \langle 90\|0\rangle)_{3s}$	MISS-4	8·8	-0.0664	-0.0734	0.0523	-0.000305
		16·16	-0.0717	-0.0759	0.0541	-0.000335
		32·32	-0.0727	-0.0753	0.0546	-0.000339
		64·64	-0.0728	-0.0746	0.0545	-0.000338
		100·100	-0.0728	-0.0743	0.0544	-0.000336
	DQM	10 ·10	-0.0576	-0.0610	0.0432	-0.000232
		18·18	-0.0650	-0.0666	0.0489	-0.000283
		26·26	-0.0678	-0.0690	0.0509	-0.000301
		34·34	-0.0692	-0.0703	0.0519	-0.000311
		42·42	-0.0705	-0.0715	0.0527	-0.000320
	S4R	100·100	-0.0720	-0.0740	0.0541	-0.000335
$(90 \pm \langle 0\|45\rangle)_{3s}$	MISS-4	8·8	-0.0050	-0.0751	0.0013	-0.000148
		16·16	-0.0047	-0.0781	0.0005	-0.000158
		32·32	-0.0047	-0.0788	0.0002	-0.000158
		64·64	-0.0047	-0.0788	0.0001	-0.000158
		100·100	-0.0047	-0.0788	0.0001	-0.000158
	DQM	10 ·10	-0.0048	-0.0777	0.0015	-0.000154
		18·18	-0.0047	-0.0785	0.0007	-0.000157
		26·26	-0.0047	-0.0786	0.0004	-0.000157
		34·34	-0.0047	-0.0786	0.0003	-0.000157
		42·42	-0.0047	-0.0786	0.0001	-0.000157
	S4R	100·100	-0.0042	-0.0788	0.00004	-0.000159

Table 5: Test 3: Stress resultants and transverse displacement at midpoint of the VAT plates: $(0 \pm \langle 45|0\rangle)_{3s}$, $(45 \pm \langle 90|0\rangle)_{3s}$ $(90 \pm \langle 0|45\rangle)_{3s}$ subjected to unit pressure loading on the top surface and simply supported boundary conditions.

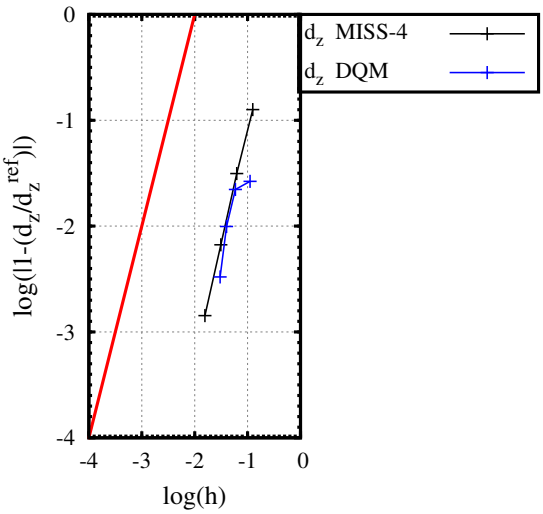

Figure 7: Test 3: Convergence of displacement d_z at the midpoint of the VAT plate $(0 \pm \langle 45|0\rangle)_{3s}$ subjected to load surface and simply supported boundary conditions. d_z^{ref} is the reference value obtained using very fine mesh/grid. h is the dimension of the mesh/grid. The red line represent h^2 convergence which is shown for reference.

4.4. Buckling analysis

The first four buckling loads four the plate under compression are reported in Table 6 and the convergence curves are shown in Fig. (8). A comparison of the MISS-4, DQM and S4R first buckling mode for the laminate $(0 \pm \langle 45|0\rangle)_{3s}$ is reported in Fig. (9), and the four first eigenvectors for the three laminates are reported in Figs. (10), (11) and (12). The MISS-4 element shows a convergence rate of h^2, with a comparable convergence rate and error to that of the DQM solution. Furthermore, all buckling results are very close to the S4R results from Abaqus.

As stated previously, the slight differences in the results for the MISS-4 and DQM buckling solutions is partly due to the difference in accounting for shear deformation. Furthermore, the MISS-4 element is based on a mixed energy formulation whereas the DQM model is a pure displacement-based approach. Thus, some difference in the convergence rate and final converged values is to be expected.

The same considerations are valid for the buckling of the plate under in-plane shear loading. For this test the evaluation of the first four buckling loads is reported in Table 7 and the convergence curves for MISS-4 and DQM are shown in Fig. (13). As for the previous test case, an h^2 convergence rate is observed for the buckling loads.

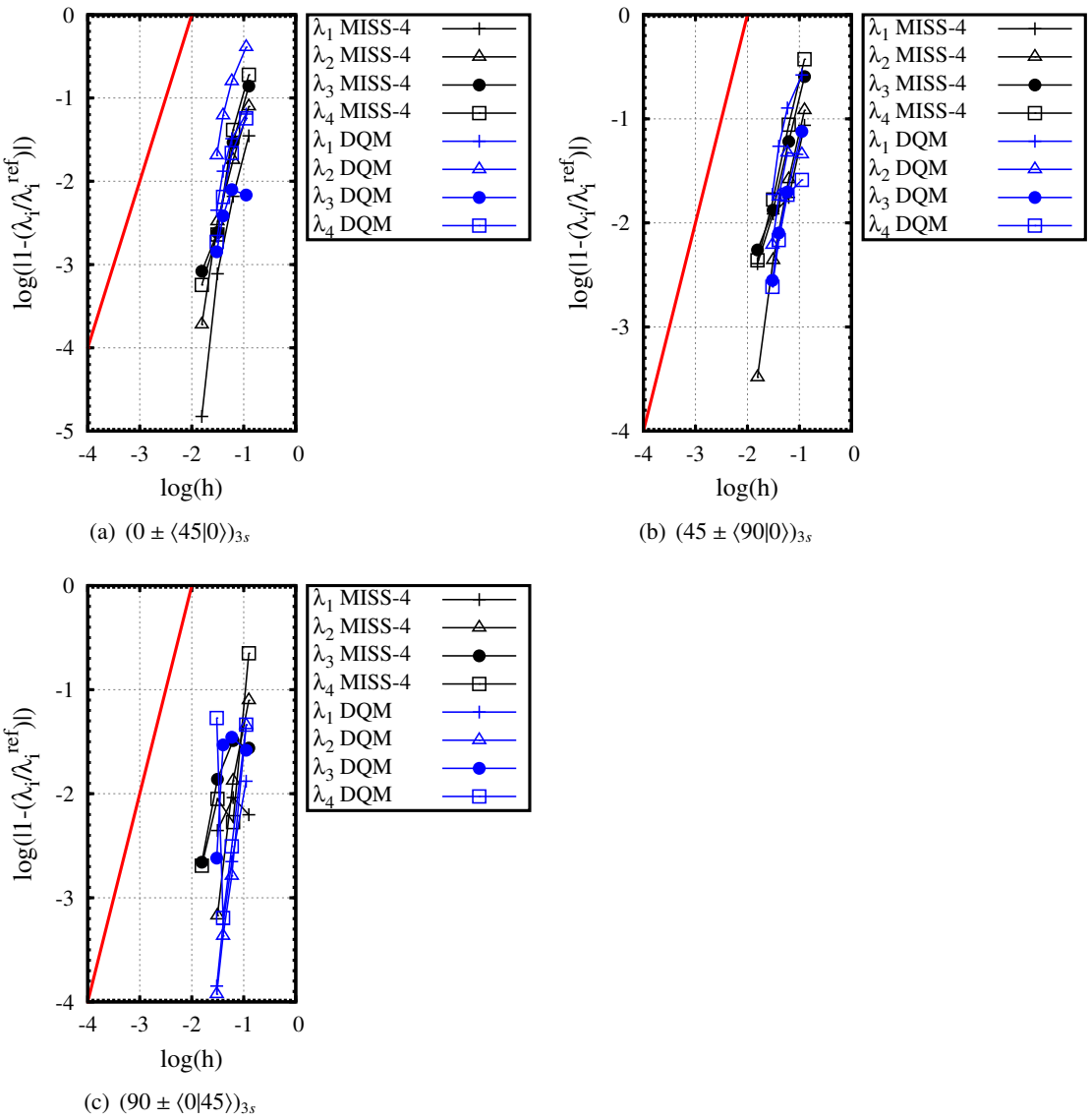

(a) $(0 \pm \langle 45|0 \rangle)_{3s}$

(b) $(45 \pm \langle 90|0 \rangle)_{3s}$

(c) $(90 \pm \langle 0|45 \rangle)_{3s}$

Figure 8: Test 1: Convergence of buckling loads $\lambda_i, i = 1 \ldots 4$ of a square VAT plate subjected to mono-axial compression and simply supported boundary conditions obtained using MISS-4 and DQM. λ_i^{ref} is the reference value obtained using very fine mesh/grid. h is the characteristic dimension of the mesh/grid and the red line representsh^2 convergence which is shown for reference.

Test 1		Mesh/Grid	λ_1	λ_2	λ_3	λ_4
$(0 \pm \langle 45\|0\rangle)_{3s}$	MISS-4	8·8	711.3	1980.9	2888.6	3831.2
		16·16	691.7	1868.7	2610.2	3352.5
		32·32	687.7	1841.7	2542.2	3226.5
		64·64	687.2	1836.0	2538.1	3220.9
		100·100	687.2	1835.7	2536.0	3219.1
	DQM	10 ·10	638.0	1045.5	2511.6	3019.5
		18·18	659.6	1486.5	2508.8	3132.0
		26·26	672.7	1658.2	2519.2	3181.2
		34·34	678.7	1731.1	2525.3	3196.0
		42·42	681.7	1767.2	2528.9	3202.0
	S4R	100·100	682.45	1821.5	2519.0	3186.8
$(45 \pm \langle 90\|0\rangle)_{3s}$	MISS-4	8 ·8	416.5	751.9	1463.6	2484.8
		16·16	448.1	688.4	1237.3	1968.3
		32·32	450.5	673.8	1182.2	1839.6
		64·64	454.3	671.0	1173.1	1817.2
		100·100	456.1	670.8	1166.7	1809.3
	DQM	10 ·10	615.9	652.3	1085.5	1763.7
		18·18	549.4	715.6	1197.7	1844.4
		26·26	514.0	695.5	1183.8	1823.0
		34·34	496.6	687.5	1177.7	1815.0
		42·42	487.4	683.3	1174.4	1810.6
	S4R	100·100	458.01	667.50	1158.2	1789.3
$(90 \pm \langle 0\|45\rangle)_{3s}$	MISS-4	8·8	831.8	997.3	1215.4	1537.0
		16·16	832.9	936.6	1221.2	1257.9
		32·32	833.3	924.9	1199.2	1231.9
		64·64	837.0	924.3	1185.5	1239.0
		100·100	837.0	924.3	1182.9	1245.7
	DQM	10 ·10	833.2	887.1	1213.5	1192.3
		18·18	846.2	930.9	1223.9	1253.8
		26·26	844.8	929.8	1217.4	1250.7
		34·34	844.4	929.5	1185.5	1183.1
		42·42	844.3	929.4	1182.6	1249.9
	S4R	100·100	833.57	918.89	1174.0	1235.7

Table 6: Test 1: Buckling loads for the VAT plates: $(0\pm\langle 45|0\rangle)_{3s}$, $(45\pm\langle 90|0\rangle)_{3s}$ $(90\pm\langle 0|45\rangle)_{3s}$ subjected to mono-axial compression and simply supported boundary conditions.

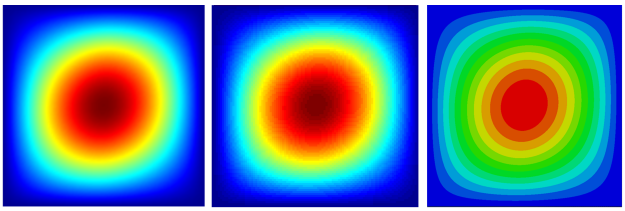

Figure 9: Test 1: Buckling mode shape of a square VAT plate $(0 \pm \langle 45|0\rangle)_{3s}$ subjected to mono-axial compression and simply supported boundary conditions (a) MISS4, (b) DQM and (c) S4R (Abaqus).

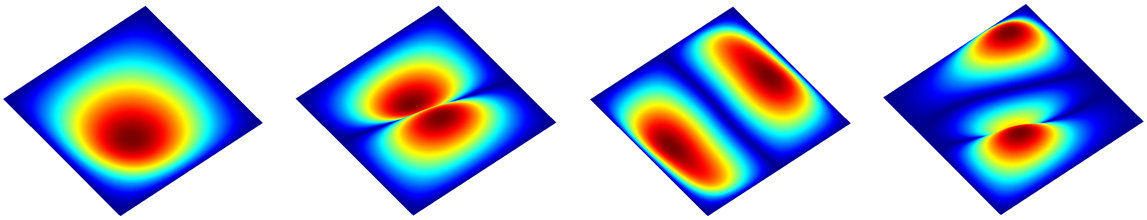

Figure 10: Test 1: Buckling mode shapes of a square VAT plate $(0 \pm \langle 45|0\rangle)_{3s}$ subjected to mono-axial compression and simply supported boundary conditions.

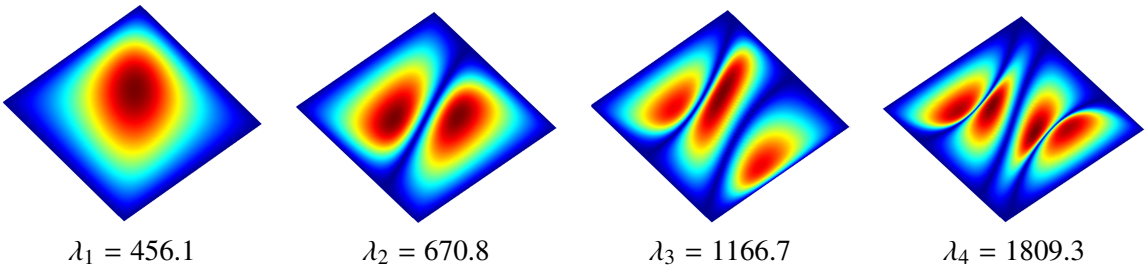

Figure 11: Test 1: Buckling mode shapes of a square VAT plate $(45 \pm \langle 90|0\rangle)_{3s}$ subjected to mono-axial compression and simply supported boundary conditions.

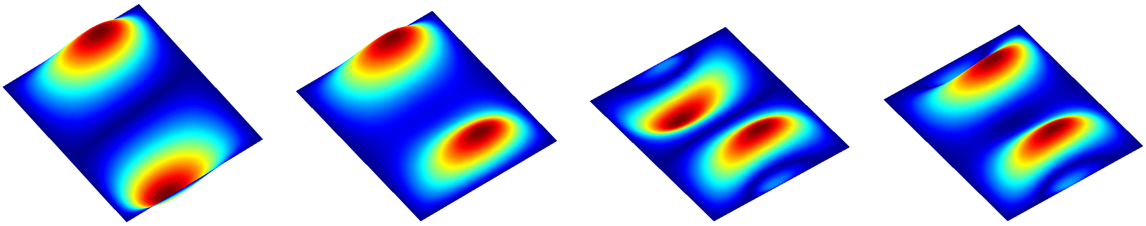

$\lambda_1 = 837.0$ $\lambda_2 = 924.3$ $\lambda_3 = 1182.9$ $\lambda_4 = 1245.7$

Figure 12: Test 1: Buckling mode shapes of a square VAT plate $(90 \pm \langle 0|45 \rangle)_{3s}$ subjected to mono-axial compression and simply supported boundary conditions.

Test 2		Mesh/Grid	λ_1	λ_2	λ_3	λ_4
$(0 \pm \langle 45\|0\rangle)_{3s}$	MISS-4	8·8	2521.4	3188.7	7194.9	9504.3
		16·16	2297.0	2790.8	5195.3	6505.6
		32·32	2242.7	2695.1	4781.0	5878.5
		64·64	2230.6	2672.4	4684.8	5732.6
		100·100	2228.5	2668.3	4666.9	5704.9
	DQM	10 ·10	2496.4	2151.4	5738.6	6260.1
		18·18	2154.7	2576.6	4666.8	5613.4
		26·26	2187.2	2620.5	4661.5	5650.6
		34·34	2203.2	2639.2	4660.8	5667.1
		42·42	2211.9	2648.7	4660.8	5675.5
	S4R	100·100	2215.2	2651.8	4637.1	5666.9
$(45 \pm \langle 90\|0\rangle)_{3s}$	MISS-4	8·8	1247.1	1328.9	3854.2	4256.1
		16·16	986.5	1051.1	2657.8	2732.5
		32·32	934.9	985.0	2220.6	2262.3
		64·64	928.0	969.2	2126.6	2155.2
		100·100	928.9	966.2	2111.6	2135.2
	DQM	10 ·10	757.8	977.0	1085.6	1920.8
		18·18	975.1	1088.0	2024.5	2277.3
		26·26	967.7	1028.4	2123.5	2237.9
		34·34	966.8	998.5	2122.0	2198.4
		42·42	965.96	972.54	2123.2	2162.9
	S4R	100·100	932.17	960.24	2111.3	2123.4
$(90 \pm \langle 0\|45\rangle)_{3s}$	MISS-4	8·8	1909.8	2050.7	4336.6	4941.4
		16·16	1711.7	1779.8	2983.2	3230.4
		32·32	1666.1	1720.0	2733.5	2906.8
		64·64	1657.2	1707.6	2679.4	2833.3
		100·100	1656.1	1705.7	2670.0	2819.3
	DQM	10 ·10	1904.5	2044.6	4334.4	4903.4
		18·18	1708.3	1777.4	2981.0	3220.3
		26·26	1664.2	1718.7	2731.8	2902.6
		34·34	1656.1	1706.8	2678.2	2831.1
		42·42	1655.2	1705.1	2668.8	2817.8
	S4R	100·100	1643.1	1692.1	2648.9	2794.9

Table 7: Test 2: Buckling loads for the VAT plates $(0 \pm \langle 45|0\rangle)_{3s}$, $(45 \pm \langle 90|0\rangle)_{3s}$ $(90 \pm \langle 0|45\rangle)_{3s}$ subjected to in-plane shear loading and simply supported boundary conditions.

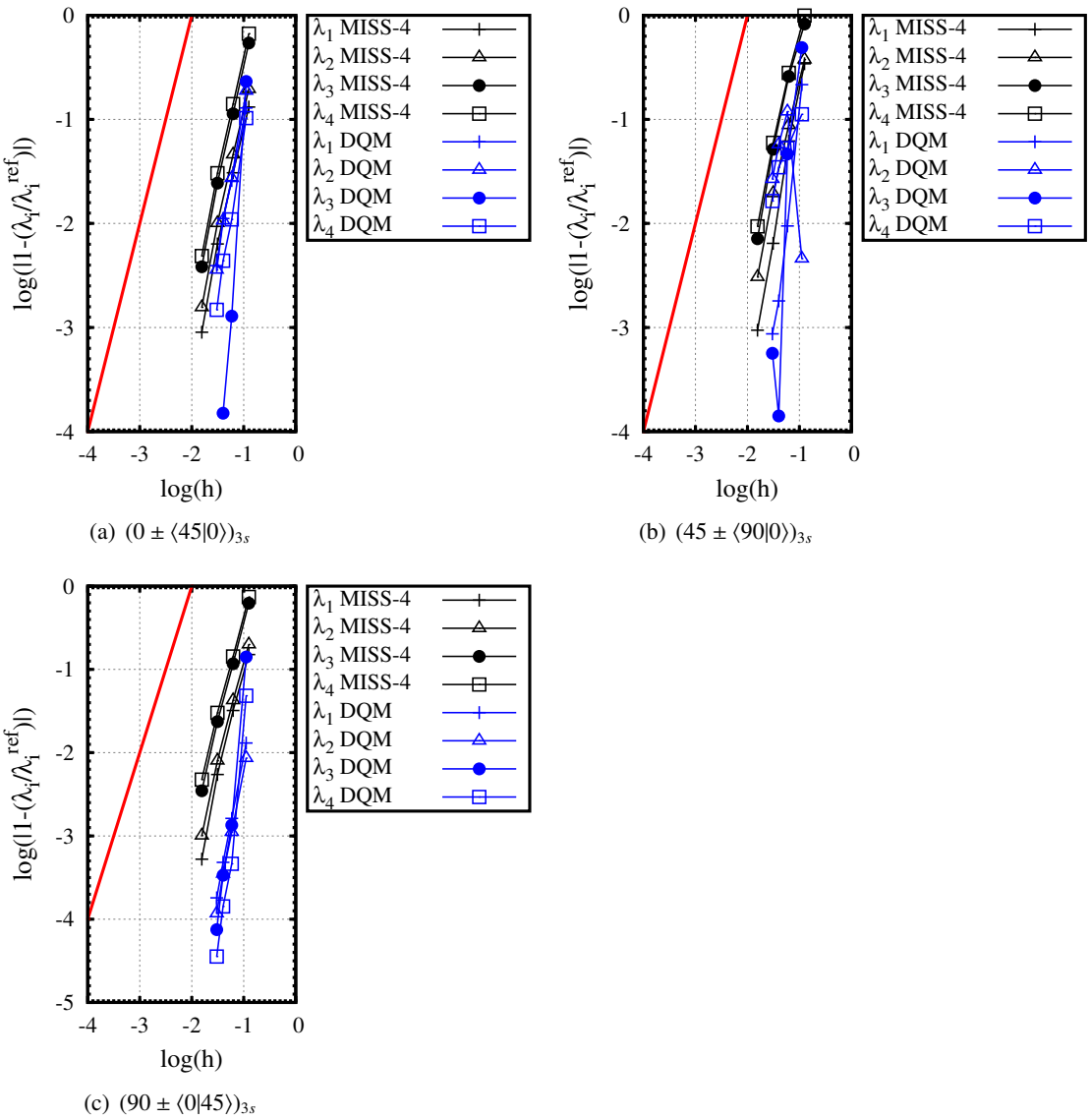

(a) $(0 \pm \langle 45|0 \rangle)_{3s}$

(b) $(45 \pm \langle 90|0 \rangle)_{3s}$

(c) $(90 \pm \langle 0|45 \rangle)_{3s}$

Figure 13: Test 2: Convergence of buckling loads $\lambda_i, i = 1 \ldots 4$ of the square VAT plate subjected to shear load and simply supported boundary conditions obtained using MISS-4 and DQM. λ_i^{ref} is the reference value obtained using very fine mesh/grid. h is the dimension of the mesh/grid and the red line represents h^2 convergence which is shown for reference.

5. CONCLUDING REMARKS

A mixed finite element MISS-4 for the linear static and buckling analysis of VAT plates has been presented and its performance in terms of accuracy and convergence rate evaluated. An h^2 convergence, i.e. to the square of the element characteristic dimension, has been shown for both static linear and buckling analyses, and this quadratic convergence leads to small numerical errors even for rough meshes. Comparisons with the more efficient Differential Quadrature Method (DQM), which exhibits strong performance in terms of convergence rate and numerical errors, as well as the S4R element in Abaqus confirms that the numerical solutions via the proposed MISS-4 finite element is comparable with benchmarks often used in the literature.

Thus, the beneficial characteristics of the corotational finite element framework in terms of computer implementation, feasibility, robustness, convergence and error control have been documented within a VAT context. Future work will focus on extending the analysis into the post-critical regime using Koiter's asymptotic approach and using Monte Carlo engines to study possible imperfection insensitivity of VAT structures.

Acknowledgement

The authors from University of Calabria wish to acknowledge the *International Network for the Exchange of Good Practices in Innovative, Seismically Safe and Eco-friendly Buildings* (POR-FSE CALABRIA 2007-2013 RISPEISE) for the financial support. The authors from the University of Bristol would like to acknowledge the support by the Engineering and Physical Sciences Research Council through the EPSRC Centre for Doctoral Training in Advanced Composites [grant number EP/G036772/1] at the University of Bristol.

BIBLIOGRAPHY

References

[1] Casciaro R. Computational asymptotic post-buckling analysis of slender elastic structures. Phenomenological and Mathematical Modelling of Structural Instabilities, Springer Vienna 2005; 470: 195-276.

[2] Wu Z, Raju G, Weaver PM. Framework for the Buckling Optimization of Variable-Angle Tow Composite Plates. AIAA Jounral, 2015; 53: 3788-3804.

[3] Fu X, Ricci, S, Bisagni C. Minimum-weight design for three dimensional woven composite stiffened panels using neural networks and genetic algorithms. Compos Struct, 2015; 134: 708-715.

[4] Barkanow E, Eglitis E, Almeida F, Bowering MC, Watson G. Optimal design of composite lateral wing upper covers. PartII:Nonlinear buckling analysis. Aerospace Science and Technology, 2016; 51: 87-95.

[5] Nguyen XH, Kim N, Lee J. Optimum design of thin-walled composite beams for flexural-torsional buckling problem. Compos Struct, 2015; 132: 1065-1074.

[6] Henrichsen SR, Lindgaard E, Lund E. Robust buckling optimization of laminated composites tructures using discrete material optimization considering 'worst' shape imperfections. Thin Walled Struct, 2015; 94: 624-635.

[7] Bacarezza O, Aliabadi MH, Apicella A. Robust design and optimization of composite stiffened panels in post-buckling. Struct Multidisc Optim, 2015; 51:409-422.

[8] Salerno G, Casciaro R. Mode Jumping and attractive paths in multimode elstic buckling. Int J Numer Methods Eng, 1997; 40(5): 833-861.

[9] Barbero EJ, Madeo A, Zagari G, Zinno R, Zucco G. Imperfection sensitivity analysis of composite cylindrical shells using Koiter's method. 3rd International Conference on Buckling and Postbuckling Behaviour of Composite Laminated Shell Structures with DESICOS Workshop, 2015; Braunschweig, Germany.

[10] Barbero EJ, Madeo A, Zagari G, Zinno R, Zucco G. Imperfection sensitivity analysis of laminated folded plates. Thin Walled Struct, 2015; 90: 128-139.

[11] Casciaro R, Mancusi G. Imperfection sensitivity due to coupled local instability: a non-convex QP solution algorithm. Int J Numer Methods Eng, 2006; 67(6): 815-840.

[12] Pignataro M, Di Carlo A, Casciaro R. On nonlinear beam models from the point of view of computational post-buckling analysis. Int J Solids Struct, 1982; 18(4): 327-347.

[13] Garcea G, Madeo A, Casciaro R. The implicit corotational method and its use in the derivation of nonlinear structural models for beams and plates. J Mech Mat Struct, 2012; 7(6): 509-538.

[14] Garcea G, Madeo A, Casciaro R. Nonlinear FEM analysis for beams and plate assemblages based on the implicit corotational method. J Mech Mat Struct, 2012; 7(6): 539-574.

[15] Garcea G, Madeo A, Zagari G, Casciaro R. Asymptotic post-buckling FEM analysis using corotational formulation. Int J Solids Struct, 2009; 46(2): 377-397.

[16] Zagari G, Madeo A, Casciaro R, de Miranda S, Ubertini F. Koiter analysis of folded structures using a corotational approach. Int J Solids Struct, 2013; 50(5): 755-765.

[17] Garcea G, Salerno G, Casciaro R. Sanitizing of locking in Koiter perturbation analysis through mixed formulation. Comput Method Appl M 1999; 180: 137-167.

[18] Garcea G, Salerno G, Casciaro R. Extrapolation locking and its sanitization in Koiter's asymptotic analysis. Comput Meth Appl Mech Eng, 1999; 180: 137-167.

[19] Kim BC, Potter K, Weaver PM. Continuous tow shearing for manufacturing variable angle tow composites. Compos Part A, 2012; 43(8): 1347-1356.

[20] Cooper AAG. Trajectorial fiber reinforcement of composite structures. Department of Mechanical and Aerospace Engineering, Washington University 1972.

[21] Gurdal Z, Olmedo R. In-plane response of laminates with spatially varying fibre orientations: variable stiffness concept. AIAA J, 1993; 31(4): 751.

[22] Gurdal Z, Tatting BF, Wu CK. Variable stiffness composite panels: Effects of stiffness variation on the in-plane and buckling response. Composites Part A: Applied Science and Manufacturing, 2008; 39: 9118-922.

[23] Setoodeh S, Abdalla MM, Ijsselmuiden ST, Gurdal Z. Design of variable stiffness composite panels for maximum buckling load. Compos Struct, 2008; 87: 109-117.

[24] Lopes CS, Gurdal Z, Camanho PP. Tailoring for strength of composite steered-fiber panels with cutouts. Composites Part A: Applied Science and Manufacturing, 2010; 41: 1760-1767.

[25] Wu Z, Weaver P M, Raju G, Kim B C. Buckling analysis and optimization of variable angle tow composite plates. Thin Walled Struct, 2012; 60: 163-172.

[26] Raju G, Wu G, Kim BC, Weaver PM. Prebuckling and buckling analysis of variable angle tow plates with general boundary conditions. Compos Struct, 2012; 94: 2961-2970.

[27] Raju G, Wu Z, Weaver PM. Buckling and postbuckling of variable angle tow composite plates under in-plane shear loading. Int J Solids Struct, 2015; 58: 270-287.

[28] Coburn BH, Wu Z, Weaver PM. Buckling analysis of stiffened variable angle tow panels. Compos Struct, 2014; 111: 259-270.

[29] Wu Z, Raju G, Weaver PM. Postbuckling analysis of varible angle tow composite plates. Int J Solids Struct, 2013; 50: 1770-1780.

[30] Wu Z, Weaver PM, Raju G. Postbuckling optimisation of variable angle tow composite plates. Compos Struct, 2013; 103: 34-42.

[31] White SC, Weaver PM. Towards imperfection insensitive buckling response of shell structures-shells with plate-like post-buckled responses. Proceedings of the 4th Aircraft Structural Design Conference of the Royal Aeronautical Society, 2014; Belfast, UK.

[32] Ijsselmuiden ST, Abdalla MM, Gurdal Z. Optimization of variable-stiffness panels for maximum buckling load using lamination parameters. Journal of Aircraft, 2010; 48(1): 134-143.

[33] van Campen JMJF, Kassapoglou C, Gurdal Z. Generating realistic laminate fiber angle distributions for optimal variable stiffness laminates. Composites Part B: Engineering, 2012; 43: 354-360.

[34] Arian Nik M, Fayazbakhsh K, Pasini D, Lessard L. Surrogate-based multi-objective optimization of a composite laminate with curvilinear fibres. Compos Struct, 2012; 94: 2306-2313.

[35] Arian Nik M, Fayazbakhsh K, Pasini D, Lessard L. Optimization of variable stiffness composites with embedded defects induced by Automated Fiber Placement. Compos Struct, 2014; 107: 160-166.

[36] Yazdani S, Ribeiro P, Rodrigues J D. A p-version layerwise model for large deflection of composite plates with curvilinear fibres. Compos Struct, 2014; 108: 181-190.

[37] Yazdani S, Ribeiro P. A layerwise p-version finite element formulation for free vibration analysis of thick composite laminates with curvilinear fibres. Compos Struct, 2015; 120: 531-542.

[38] Akhavan S, Ribeiro P. Natural modes of vibration of variable stiffness composite laminates with curvilinear fibers. Compos Struct, 2011; 93(11): 3040-3047.

[39] Groh RMJ, Weaver PM, White SC, Raju G, Wu Z. A 2D equivalent single-layer formulation for the effect of transverse shear on laminated plates with curvilinear fibres. Compos Struct, 2013; 100: 464-478.

[40] Groh RMJ, Weaver PM. Buckling analysis of variable angle tow variable thickness panels with transverse shear effects. Compos Struct, 2014; 107: 482-493.

[41] Raju G, Wu Z, Weaver PM. Postbuckling analysis of variable angle tow plates using differential quadrature method. Compos Struct, 2013; 106: 74-84.

[42] White SC, Raju G, Weaver PM. Initial post-buckling of variable-stiffness curved panels. Journal of the Mechanics and Physics of Solids, 2014; 71: 132-155.

[43] Groh RMJ, Weaver PM. Mass Optimization of Variable Angle Tow, Variable Thickness Panels with Static Failure and Buckling Constraints, AIAA SciTech 56th AIAA/ASCE/AHS/ASC Structures, Structural Dynamics, and Materials Conference 2015, Kissimmee, USA.

[44] Tornabene F, Fantuzzi N, Ubertini F, Viola E. Strong formulation finite element method based on differential quadrature: A survey. Appl Mech R, 2015; 67: 1-55.

[45] Raju G, White S, Wu Z. Optimal postbuckling design of variable angle tow composites using lamination parameters. Proceedings of the 56th AIAA/ASME/ASCE/AHS/ASC Structures, Structural Dynamics and Materials Conference, 2015; Kissimmee, USA.

[46] Tornabene F, Fantuzzi N, Bacciocchi M. Higher-order structural theories for the static analysis of doubly-curved laminated composite panels reinforced by curvilinear fibers. Thin Walled Struct, 2016; 102: 222-245.

[47] Tornabene F, Fantuzzi N, Bacciocchi M, Viola E. Higher-order theories for the free vibrations of doubly-curved laminated panels with curvilinear reinforcing fibers by means of a local version of the GDQ method. Compos Part B-Eng, 2015; 81: 196-230.

[48] Madeo A Zagari G Casciaro R de Miranda S. A mixed 4-node 3D plate element based on self-equilibrated isostatic stresses. Int J Struct Stab Dyn, 2013; 15(4).

[49] Barbero EJ, Madeo A, Zagari G, Zinno R, Zucco G. A mixed isostatic 24 dof element for static and buckling analysis of laminated folded plates. Compos Struct, 2014; 116: 223-234.

[50] Madeo A, Zagari G, Casciaro R. An isostatic quadrilateral membrane finite element with drilling rotations and no spurious modes. Finite Elem Anal Des, 2012; 50: 21-32.

[51] Hibbitt, Karlsson, and Sorensson. Abaqus theory manual, version 6.8. Dassault, 2009.

[52] Reddy JN. Mechanics of Laminated Composite Plates and Shells - Theory and Analysis Boca Raton: CRC Press, 2004.

[53] Barbero EJ. Introduction to composite materials design–Second Edition. Boca raton, FL: CRC Press, 2010.

[54] MATLAB. The Mathworks. Boston, MA, 2013.

[55] Auricchio F, Sacco E. A mixed-enhanced finite-element for the analysis of laminated composite plates. Int J Numer Methods Eng, 1999; 44: 1481-1504.

[56] Laitinen M, Lahtinen H, Sjölind S G. Transverse shear correction factors for laminates in cylindrical bending. Commun Numer Methods in Eng, 1995; 11(1): 41-47.

[57] Bilotta A, Casciaro R. Assumed stress formulation of high order quadrilateral elements with an improved in-plane bending behaviour. Comput Meth Appl Mech Eng, 2002; 191(15-16): 1523-1540.

[58] Pian THH, Sumihara K. Rational approach for assumed stress finite elements. Int J Numer Methods Eng, 1984; 20(9): 1685-1695.

[59] Ritto-Corrêa M, Camotim D. On the differentiation of the Rodrigues formula and its significance for the vector-like parameterization of Reissner-Simo beam theory. Int J Numer Methods Eng, 2002; 55: 1005-1032.

[60] Zienkiewicz OC, Taylor RL. The finite element method for solid and structural mechanics. 6th Edition. Elsevier Butterworth-Heinemann, 2005.

[61] Bellman R, Kashef G. Casti J. Differential quadrature: A technique for the rapid solution of nonlinear partial differential equations. Journal of Computational Physics, 1972; 10: 40-52.

[62] Shu C, Richards BE. Application of generalized differential quadrature to solve two-dimensional incompressible Navier-Stokes equations. International Journal for Numerical Methods in Fluids, 1992; 15: 791-798.

[63] Quan JR, Chang, CT. New insights in solving distributed system equations by thequadrature method. I. Analysis. Computers & Chemical Engineering, 1989; 13(7): 779-788.

[64] Shu C. Differential Quadrature and its Application in Engineering. Springer Verlag, 2000.